1) **Point by point responses to referee # 1 and referee #2.**
2) **A list of all relevant changes made in the manuscript.**
3) **A marked-up MS version**

1)

We thank referee#1 for the thorough review and very valuable feedback.

The issues stated in '**General comments**' are all taking into consideration in a revised MS.
Our main ambition with the present paper has been to show how UAV data can substitute or supplement satellite data in estimation of evapotranspiration. To do that we've flown a UAV during the growing season of 2014 with a thermal camera over a barley field where we also operate an eddy covariance tower, which could act as ground reference for fluxes and radiative parameters obtained by the UAV. Further, we've obtained surveys of LAI development during the same season. As such, we do not have detailed verification of the latent heat fluxes (e.g. heterogeneity soil properties) beyond what the changing footprint of the EC tower can provide. We can for that reason not provide ground based verification of differences within the ETa maps. We can only provide plausible explanations for these differences. Plausible explanations involve soil properties applicable to entire field and irrigation management. The spatial discussion in a revised MS will be expanded by including these aspects as shown under 'Specific comments'.

With regard to EC-footprint coverage, these overlapped entirely with UAV data except for a few cases where approx. 3% were lacking. In these cases, the lacking bit was simple obtained from the ETa maps and added in order to reach 100%. This will be stated in the revised MS.

The method section will be re-written to make the model description clearer and specific comments from P5L22-25 to P7L25-27 (regarding the method section) will all be considered.

Categorizing this MS as a 'technical note' is ok with the authors. However we will let the editor make the final decision regarding this matter.

The corrections and comments under '**Specific comments**' are applied directly to a revised MS version if issues are not touched upon in the following.

P3L2-5 & P3L5-6: Check syntax.

Section (1) has been re-written into section (2):

(1) *The significant contribution provided by the original TSEB model, is the partition of remotely sensed LST observations into two layers; a soil temperature and a canopy temperature, which enables a partition of heat flux estimations into soil and canopy respectively. The temperature partition allows the model to avoid the need for estimating the so called excess resistance term, which is difficult to derive reliably. As most of the remote sensing systems only provide a single radiometric observation, Norman et al. (1995) proposed applying an iterative process to derive the canopy and soil temperature. It is based on an initial guess of canopy transpiration, which was based on the Priestley and Taylor potential evapotranspiration (Priestley and Taylor, 1972).*

(2) *Norman et al. (1995) partitions remotely sensed LST observations into two layers; a soil temperature and a canopy temperature, using a Priestley-Taylor approximation (Priestley and Taylor, 1972). The temperature*

partition enables a partition of heat flux estimations into soil and canopy heat fluxes. Further, it eliminates the necessity of estimating the 'excess' resistance term, which is empirically determined and difficult to reliably derive. The 'excess' resistance term is used in single-layer models in order to correct for a substitution of directional radiometric temperature in place of the aerodynamic temperature when calculating sensible heat fluxes (Eq. (5), (8) and (9) in Norman et al. (1995)) The Priestley-Taylor approximation partition the divergence of net radiation in the canopy into sensible and latent heat fluxes and an initial guess of canopy transpiration is used to split LST into soil and canopy temperatures.

P3L11: The term "TSEB-PT" is not used throughout the MS

The TSEB-PT expression is used when this specific algorithm is used. The TSEB expression is used when referring to both the TSED-PT and the DTD model; the two source energy balance modelling scheme. This difference will be clarified in a revised version of the MS.

P3L18-45: Too extensive.

Line 18-45 is re-written and shortened to:

Trying to overcome this issue, Norman et al. (2000) developed the Dual-Temperature-Difference model (DTD), incorporating two temperature observations into the TSEB modelling scheme; one conducted an hour after sunrise and another conducted later the same day when flux estimations are desired. One hour after sunrise, the surface heat fluxes are minimal and observations acquired at this time represent a 'starting point' for the temperatures collected later the same day.

For agricultural and some hydrological purposes, there is a shortcoming in spatial and temporal resolution of satellite observations (Guzinski et al., 2014). *This is especially true in areas prone to overcast weather conditions, such as in northern Europe where present study is conducted, as satellite thermal infrared and visible observations cannot penetrate clouds* (Guzinski et al., 2013). *Unmanned aerial vehicles (UAVs) (or Remotely Piloted Aircraft System, RPAS, in its most recent terminology) enable a critical improvement for both spatial and temporal resolution of remotely sensed data. UAVs can operate at any specific time of day and year provided that strong wind and rainfall are absent. Therefore, the UAV platform enables data acquisition one hour after sunrise, granting inputs in better accordance with the DTD requirements and due to the relative low flying height, also during overcast conditions (Hunt Jr et al., 2005). When UAV data are combined with the presented models, spatially detailed heat flux maps can be generated and provide insight to different evapotranspiration rates and plant stress at decimeter scale.*

P5L6: What is the size of the test area?

400X600 m. The size of test area is included in section 2 of revised MS.

P5L6: Please provide information on soil properties.

The soil profile consists of an upper 0.25 m organic topsoil and course sand from topsoil and downwards. Soil porosity of the upper 1st m range between 0.35 and 0.40 and the available soil water [pF 2.0–4.2, suction pF = $\log_{10}$(suction in centimeters of water)] is 19% (v_{water}/v_{soil}) in the upper 0.20 m of the plow layer and only 6% (v_{water}/v_{soil}) in the remaining part of the root zone, necessitating frequent irrigation to maintain crop growth during growing seasons. This will be stated in the revised MS.

P5L8: 990 mm precipitation is quite a lot. Why is irrigation needed? Please describe the irrigation management in more detail.

Because of the soil properties stated above, irrigation is performed consistently throughout the growing season. In 2014 (investigated year) irrigation was performed five times: May 23^{d}, May 29th, June 5th, June 15th and June 25th. Approx. 25 mm of water was applied on each occasion. The type of irrigation system is a traveling irrigation gun that rotates. The gun is automatically pulled across

the field in tramlines that run in north-south direction, using the same pattern over the season. The irrigation tubing is wound around a steel drum as the gun moves and it has to be moved manually to a new tramline when the distance of one tramline has been traveled. Description of irrigation management will be included in the revised MS.

P5L9: These statements should be more quantitatively described (e.g. in days per year).

Average wind speed on agricultural site in 2014 was 3.8 m/s and westernly wind occurred 30% of the time. This is included in the revised MS.

Comments P5L22-P7L25-27 regarding model description, is all taken into consideration and section 3 will be re-written in order to give a more thorough review of models and to make relationships between collected data and algorithms more clear.

P9L22: What is the resulting position accuracy after correction?

Since no ground control points are used, (stated in P10L1-2) an overall position accuracy cannot be calculated. However an error of 0.5 m was attained in experiment with a single ground control point as check point in post-processing of thermal images.

P10L3-4: Figure 2 is not really needed because the ETa maps already show the resolution of the data.

We agree and figure 2 is not included in new MS.

P10L14-20: For potential users, it would be interesting to know, how much difference the different composition techniques would produce in terms of estimated ETa.

The difference between using a mean and a maximum value composition technique is approx. 0.3 Kelvin degrees and 5 Wm^{-2} latent heat flux on average for the study site. This will be included in the revised MS.

P10L29: Please show the respective EC-footprint weights in the ETa maps (e.g. using isolines). Since the ETa maps are covering very different areas, it should be analysed to which degree missing ETa information within the EC-footprints may have influenced the results.

Even though the shape and placement of the EC-footprints differs for each ETa map, the EC-footprints are within the extent of ETa maps and the cultivated area except in a few cases, see answer under 'General comments' 2). The ETa maps are the actual results and spatial pattern should stand out clear. Therefore we will map out the 90% footprint with a single line on ETa maps in order to keep spatial evapotranspiration patterns to stand out clear.

P11L9-13: Given the limitations in the model description, it is unclear how most of these data sets find their way into the modelling.

Because the TSEB-PT and the DTD model are thoroughly described in other papers e.g. Norman et al. (1995) and Guzinski et al. (2014), a detailed description of algorithms seems unnecessary in this paper. However the description of models (section 3) will be re-written and the relationship between parameters and algorithms will be enhanced.

P11L11-12: The values for these parameters used for each ETa estimation should be presented.

Values not obtained from Guzinski et al. 2014 and values that differ between each model run/ETa map will be listed in revised MS, see table below.

Date	LAI	Canopy height (m)	Green veg. fraction	$Albedo_{soil+veg.}$
10 April 2014	0.48	0.02	1	0.142
22 April 2014	0.88	0.08	1	0.181
15 May 2014	1.49	0.12	1	0.182
22 May 2014	3.90	0.30	1	0.226
18 June 2014	4.03	0.95	0.7	0.181
02 July 2014	3.43	1.10	0.3	0.202
22 July 2014	3.02	1.20	0.02	0.189

P12L22: Shouldn't the patterns be exactly the same, since no further spatial information is added?

Yes the patterns are the same, this will be stated more clearly.

P12L22-24: How will this affect the results?

This will not affect the results or the comparison between ETa maps and measurements from the eddy towers since the EC-footprints are within the final maps and the cultivated area expect a few exceptions, see answer under 'General comments' 2).

P13L1-4: The effect of tramlines should be presented in more detail. I have difficulty to spot the tramlines in the ETa maps, so please add information in the maps. You could determine differences of ETa rates.

The mentioning of differences between tramlines and areas with barley should provide a sense of how detailed the maps are. This might be unnecessary and the comparison between tramlines and barley areas will be excluded and instead this section will focus on spatial patterns as a consequence of irrigation systems and soil properties.

P13L7-8: Please provide possible reasons.

Possible reasons include soil properties which will be discussed in revised version of the MS.

P13L9: "bodes"?

We acknowledge the incorrect choice of word and 'bodes well for' will be replaced with 'demonstrates'.

P13L15-17: This is statement is rather trivial.

Following line will be deleted from revised MS: *Accurate computation of net radiation (R_n) is essential in order to satisfactory model sensible and latent heat fluxes*.

P13L19-26: As you point out, the R_n estimates include the R_s,in from the EC-station. There you should compare the R_l values, which are purely determined from UAV measurements.

Yes, comparing R_l values does give valuable insight to the quality of UAV data and a graph showing modelled vs measured R_l will be included and discussed in revised MS.

P13L27-28: This statement is difficult to comprehend. Please reformulate.

The sentence have been reformulated to*: The majority of surface on 10 April 2014 comprises of soil, which albedo and emissivity varies with water content. If the soil was comparably wetter compared to the time of albedo and emissivity estimations for model input, the LST would be underestimated.*

P14L3-8: Here you are comparing Rn not ETa. Rn is determined at the meteorological station with much higher resolution. Thus, you could compare the same measurement

periods. The variations in irradiance should be recorded by both systems, so that the average should be similar.
Yes, the nature of different measurements was confused here. Following sentence will be moved to flux section: *LST collected with UAVs are instantaneous but also a mosaic of instantaneous LST collected in a time span of 20 min. Comparing this kind of measurement to a 30 min flux average from eddy covariance system can lead to substantial disagreement.*
P14L10-11: reformulate "steadier trend prediction".
'Steadier trend prediction' is replaced by 'a better linear relation'.
P14L1516: This data should be presented.
Yes, we will include and discuss modelled vs measured G data in fig. 3 in revised MS.
P16L22: Which kind of calibration, if any, was applied in this study?
The thermal camera is used with factory calibrations.

Answer to referee#2

Thanks for valuable comments and for highlighting the importance of focusing on all components of the surface energy balance.

GENERAL COMMENTS ABOUT SOIL HEAT FLUX
In this study we use two standard models that have been tested and proven valuable in other studies, in order to investigate whether land surface temperatures collected with a UAV are of sufficient quality to give reliable results for surface energy balance components – with special focus on latent heat flux (LE). In our perspective, the study gives confidence that the DTD model in particular estimate reliable fluxes. Further the models and the spatially high resolution surface temperatu

re-input, reveal patterns in evaporation which could not have been quantified through more established techniques, such as Eddy covariance systems or with use of satellite data.

We are aware that there are shortcomings in the methodology due to spatial variations also in parameters which per se cannot be measured from UAV instrumentation, but view the study as progress towards reliable flux measurements from UAV data.

We do agree with the reviewer that some uncertainty can be associated with the estimation of the soil heat flux (G) and appreciate the comments about the time issue where intermittent cloud cover will have an effect on the measured G values, which is not presently accounted for in the MS. Weather conditions with fast changes in the radiation levels as a consequence of intermittently cloudy condition occur on four occasions during the experiment and therefor are of relevance in present study. We're facing some challenges concerning the design of the experiment on this matter because it does not allow much further interpretation of temporal variability beyond the half hourly time steps that the flux data provides. However, this time-scale issue will be mentioned and discussed in revised MS.

Further, G was measured from two heat flux plates located approximately 3 cm below the soil surface directly under the net radiometer in the plowing layer of the homogeneous sandy loam soil of the barley field. We have no direct measurements that support a spatial interpretation of the

variation in the soil heat flux, nor in the net radiation, beyond what the EC tower provides, and for that reason cannot evaluate the uncertainty associated with this.

In the model calculations of LE presented in the MS, G is not used directly from the measurements but parameterised in the two models (see Eq. 8, 9, 12 and 13 below). Both models takes into account the changing plant cover over the season and for that reason can also account for a changing proportion of radiation conducted to the top soil layers. G is hence not estimated from a fixed proportion of Rn, which we do agree could have introduced unnecessary errors. Attached Fig.1 shows the proportion of Rn on the barley field that is attributed to heating of the top soil layers, G. The proportion varies over the season as a function of the increasing plant cover, and thus we do agree that a fixed proportion would have led to errors.

In the new version of the MS we've included measured and modelled G (attached Fig. 2) which reveals that the modelled G values are lower than measured, but also that the role of G in the energy budget, and thus in the two models, has limited impact for the estimation of latent heat flux.

Model calculations of G:

TSEB PT

*S*oil heat flux is computed following Liebethal and Foken (2007):

$$G = 0.3R_{n,s} - 35 \quad (8)$$

where $R_{n,S}$ is net radiation that reaches the soil surface computed as $R_{n,S} = R_n - \Delta R_n$.

ΔR_n-definition:

$$\Delta R_n = R_n \left[1 - \exp\left(\frac{-\kappa F \Omega_0}{\sqrt{2\cos(\theta_s)}}\right)\right] \quad (9)$$

where R_n is net radiation, Ω_0 is the nadir view clumping factor that depends on the ratio of vegetation height to plant crown width which is set to 1.0, θ_s is the sun zenith angle calculated by model from time of the day, κ is an extinction coefficient varying smoothly from 0.45 for LAI more than 2 to 0.8 for LAI less than 2 and F is the total Leaf Area Index (LAI).

DTD

Computations of soil heat flux (G) differ between the two models because the difference in radiometric temperature between sunrise and midday observations in DTD can be used as an approximation of the diurnal variation in soil surface temperature. Soil heat flux computations are derived from the soil heat flux model of Santanello and Friedl (2003):

$$G = R_{n,S} A \cos\left(2\pi \frac{t+10800}{B}\right) \quad (12)$$

where t is time in seconds between the observation time and solar noon, $A = 0.0074\Delta T_R + 0.088$, $B = 1729\Delta T_R + 65013$ and ΔT_R is an approximation of the diurnal variation in the soil surface temperature from UAV data.

$$\mathrm{R}_{n,S} = R_n * \exp(-\kappa F \Omega_0) \quad (13)$$

where κ varies smoothly between 0.45 for LAI more than 2 to 0.8 for LAI less than 2, F is LAI and Ω_0 is the nadir view clumping factor.

MINOR COMMENTS

Please replace 'evapotranspiration' by 'evaporation' throughout. See, f.e., doi 10.1002/hyp.5563 for why.

Ans: The authors of this MS agree to change 'evapotranspiration' to the more simple and correct 'evaporation'. This study operates with two evaporation sources: Transpiration and evaporation from soil respectively. The term 'evaporation' will be used when evaporated water is regarded as stemming from a single source.

P7470 l27: What is 'explicates'?

'explicate' is replaced with 'outline'.

P7473 l 1: Is it not rather tens or hundreds of meters?

Ans: Thermal bands of satellites that are most often described in the academic literature such as Landsat and MODIS have spatial resolutions equal to or lower than 1000 meters. However numerous satellites collect data within the thermal spectra with spatial resolutions above 1000 meters e.g. GOES-R, GOSAT, Seasat, GMS-5, MOS-1, Electro-L. Therefore we write tens to thousands meters.

P7473: So what would you say is the main difference between your UAV/evaporation work and that of others? Would be good to say that in one sentence or so before line 25.

Ans: The authors find that the most exciting and useful frame of this work is the application of UAV platforms into new fields. We will emphasize this by rewriting the sentence before L25 into:
'However, research in possibilities and limitations of UAV platforms is still at an early stage and the present paper introduces the usage of UAV platforms into the fields of heat fluxes and hydrology.'
And a few sentences before insert the sentence:
'Here we hypothesis that UAV data can substitute satellite images and in combination with the presented heat flux models, can be used to generate spatially detailed heat flux maps that provide insight to different evaporation rates and plant stress at decimeter scale.'

P7474: Why not put 'Site description' under materials and methods instead of as a single paragraph?

Ans: In the revised MS we merge 'Site'with 'Method' under the heading 'Materials and methods'. This heading also covers paragraphs from the former 'Data description and processing'.

P7475 l15: Reference does not fit reference in reference list. This is just one my eye fell on so please check throughout or use some system that does not allow for such differences.

Ans: The g in Keijman has been deleted and references and reference list has been double-checked to ensure that such mistakes will not occur in revised MS.

P7475: I find the explanation of TSEB a bit long. If you can refer more to literature, that would not be a loss in my opinion.

Ans: The TSEB explanation has been re-structured and re-written, trying to give a better overview with only essential equations. Please see the revised 'Heat flux model' paragraph in uploaded new version of MS.

P7478: I find "Data description and processing" a strange heading and it contains a1 mix of methods and results. Please redistribute accordingly for it does not help the reader to be going back and forth between the two.
Ans: The former "Data description and processing" paragraph is now covered in the 'Materials and methods' paragraph (see answer under P7474). Further the following section has been moved to 'Results and discussion':
'The view zenith angle (Sect. 3.1) of ortho-mosaics was set to 0° for all pixels, hence the largest possible amount of soil was assumed visible. The maximum view zenith angle of the thermal camera is 15° and setting a theoretical view zenith angle to 0° could lead to a small overestimation of latent heat flux. Using a maximum value composition when generating thermal ortho-mosaics may have accommodated any bias due to 0° view zenith angle in models. However, a mean value composition was used because the mosaics produced with this method compared well with mosaics produced manually in which the edges of the images were eliminated due to vignetting effects. Using a mean value composition is thus assumed to enable the usage of entire images without eliminating or correcting vignetting edges and hence allowing a larger coverage and image overlap. The difference between using a mean and a maximum value composition was approx. 0.3° Kelvin and 5 W m^{-2} evapotranspiration on average for the study site.

P7480 l 25-29: This paragraph is rather unclear. Please rewrite.
Section:
'However, a mean value composition was used because the mosaics produced with this method compared well with mosaics produced manually in which the edges of the images were eliminated due to vignetting effects. Using a mean value composition is thus assumed to enable the usage of entire images without eliminating or correcting vignetting edges and hence allowing a larger coverage and image overlap. The difference between using a mean and a maximum value composition was approx. 0.3° Kelvin and 5 W m^{-2} evapotranspiration on average for the study site.'
Has been rewritten into:
'However, a mean value composition was used because the mosaics produced with this method compared well with mosaics produced manually in which the edges of each image were removed. Edges were removed in order to eliminate the vignetting effect which generally affects particularly thermal images and therefor also the images collected in this study. Using a mean value composition is thus assumed to enable the usage of entire images without eliminating or correcting for vignetting effects. Using entire images allow a larger image overlap which is crucial when images are mosaicked in Photoscan. The difference between using a mean and a maximum value composition was approx. 0.3° Kelvin and 5 W m^{-2} latent heat flux for mosaic from 10 April 2014.'

P7481 l2: 'value' and 'has' seems more correct.
Ans: Yes, 'values' and 'have' have been replaced by 'value' and 'has'.

P7481 l18: 'is' should be 'was'
Ans: Yes, done.

P7482 l17: Please include a good reference for EddyPro.
Ans: This paper will serve as reference: Fratini, G. and Mauder, M.: Towards a consistent eddy-covariance processing: an intercomparison of EddyPro and TK3, Atmospheric Meas. Tech., 7(7), 2273–2281, doi:10.5194/amt-7-2273-2014, 2014.

P7482 l28: Unclear sentence, mainly due to the fact that there is no clear agent behind 'applying' (dangling modifier).
Ans: The sentence is now:
'*When applying the surface energy balance expression any residual was assigned to latent heat flux, as recommended by Foken et al. (2011).'*

P7483 l25: 'likely to contain'
Ans: The sentence in L25 is now:
'These areas, likely to contain less healthy plants will have higher LST and produce lower rates of evapotranspiration.'
(Mistake in answer - it should have said: '*These areas likely consist of less healthy plants which will generate higher LST and lower rates of evaporation.*')

P7486: In general, the paper is well written but this page needs some re-writing. There are again these dangling modifiers without agents ibn lines 3 and 12. Lines 20-25 is a good example of a run-on sentence.
Ans: P7486 has been re-written in general. Re-writing of lines 3, 12 and 20-25 is shown below:
'*Comparing statistical parameters in this study to the study made by Guzinski et al. (2014) on the same field site with the same models but driven by satellite data, similar results are seen when only Landsat images are used. Guzinski et al. (2014) obtained RMSE values of 46 W m^{-2} for R_n, 56 W m^{-2} for H and 66 W m^{-2} for LE, obtained using TSEB-PT and Landsat data (Table 2, column ND_H in Guzinski et al. (2014)) which are comparable to RMSE values of 44 W m^{-2} for R_n, 59 W m^{-2} for H and 67 W m^{-2} for LE, obtained using DTD in this study'*
Have been re-written into:
'*Guzinski et al. (2014) applied their TSEB-PT study to the same field site as the present study but they used thermal satellite images from Landsat as boundary conditions as oppose to thermal UAV images. A comparison between these two studies shows similar accurate result. Guzinski et al. (2014) achieve RMSEs of 46 W m^{-2} for R_n, 56 W m^{-2} for H and 66 W m^{-2} for LE (Table 2, column ND_H in Guzinski et al. (2014)). This study achieves RMSEs of 44 W m^{-2} for R_n, 59 W m^{-2} for H and 67 W m^{-2} for LE, using the DTD model*.'

And:
'*Also, when comparing results in this study with those computed with the original DTD model (Norman et al., 2000) and several other studies seeking to estimate surface energy balance components from remotely sensed data (Colaizzi et al., 2012; Guzinski et al., 2013; Norman et al., 2000), the results in the present study are in the same order of agreement.'*
Has been re-written into:
'*Further, a comparison between this study and other studies seeking to estimate surface fluxes from remotely sensed data (such as Colaizzi et al. (2012); Guzinski et al. (2013); Norman et al. (2000)) show that measured and modelled fluxes are in same order of agreement*'.

And:
'The majority of data is retrieved under cloudy or overcast conditions. Data collected during sunny conditions are enclosed by black circles in Fig. 3A-C. Fluxes from sunny, cloudy and overcast days cannot immediately be categorized as being different from one another when looking at Fig. 3A-C. Table 5 shows statistical parameters calculated using only data from days with cloudy or overcast weather conditions. RMSE and MAE are better for both R_n H and LE for both models, except for the MAE and MAE as percentage of measured fluxes for H computed with TSEB-PT which increased to 50 W m^{-2} from 49 W m^{-2} and to 78 % from 52 % respectively. r values for R_n are

almost alike for data only including cloudy and overcast conditions and data also including sunny condition with values of 0.99 and 0.98 respectively. r is worse for H but better for LE for both models when looking at data that only includes cloudy and overcast conditions, see Table 4 and 5. Statistical parameters presented in Table 5 and the overall good results in the present study compared to above mentioned studies using satellite data (hence data collected in sunny conditions), validate the application of TSEB-PT and DTD models in cloudy and overcast weather conditions.'
Have been re-written into:
'*Contrary to studies using satellite images, the majority of data in this study is retrieved under cloudy or overcast conditions. Data collected during sunny conditions are enclosed by black circles in Fig. 3A-C and Table 5 shows statistical parameters calculated using only data from days with cloudy or overcast weather conditions. Based on Fig. 3A-C and on a comparison between statistical parameters in Table 4 og 5, no significant difference can be seen between data collected during cloudy, overcast and sunny weather conditions. It is thus concluded that the TSEB modelling scheme can be applied to data obtained in all three weather types.*'

P7487 l6: Would 'concatenated' not be better than 'generated'?
Ans: Yes, 'concatenated' is used in revised MS.

P7487 l15: Instead of 'Comparing' you could say A comparison…reveals that…
Ans: The sentence has been rewritten into:
'*A comparison between present results and results from other studies estimating surface energy fluxes from heat flux models and remotely sensed LST, reveal that…'*

2)

List of all relevant changes made in the manuscript:

- Description of models has been re-written and re-structured. Referee # 1 and #2 were divided regarding the degree of detail that the model description had to include. We have chosen not to present all equations in the TSEB modelling scheme as this has been done in several other papers and only present the equations of relevance for our specific purpose: Illustrating that temperatures collected with a UAV could serve as boundary condition when estimating heat fluxes with the TSEB modelling scheme. We hope that both referees will find the re-structured version satisfactory. We think the revised description gives a better overview because it is structured in the sequence the equations are executed during simulations, and further that it provides a better understanding of how field observations are applied in the models.
- Results are discussed more thoroughly. For example by comparing measured and modelled net long wave radiation and including subjects such as atmospheric emissivity and potential consequence of intermittent cloud cover.
- Soil heat flux (G) is included in results presentation and discussion.
- Description of soil properties for the overall area investigated is expanded.
- This study does not have access to data with same spatial resolution as model output maps that could have validated the evaporation patterns. However the irrigation system applied to the barley field constitutes valid explanation for patterns (and spatiotemporal changes in patterns) seen in maps. Therefore a more elaborate explanation of irrigation system is provided in the revised MS, including why irrigation is needed, the amount of irrigation, and the type of irrigation system that is applied to the field. Further a figure is presented showing the tramlines in which irrigation guns run, showing there is a high degree of coincidence between evaporation patterns and repeated patterns of irrigation.
- LE maps now also illustrate the differences between coverage of EC-footprint for each flight. A description is included of how any disagreement between map extension and EC-footprint coverage are dealt with.

3)

Estimating evaporation with thermal UAV data and two source energy balance models.

H. Hoffmann[1], H. Nieto[2], R. Jensen[1], R. Guzinski[1,*], P. Zarco-Tejada[2] and T. Friborg[1]

[1]{Department of Geosciences and Natural Resource Management, University of Copenhagen, Øster Voldgade 10, 1350 Copenhagen, Denmark}

[2]{Instituto de Agricultura Sostenible (IAS), Consejo Superior de Investigaciones Científicas (CSIC), Campus Alameda del Obispo, Av. Menéndez Pidal s/n, 14004 Córdoba, Spain}

[*]{now at: DHI GRAS, Agern Allé 5, 2970 Hørsholm, Denmark}

Correspondence to: H. Hoffmann (helene.hoffmann@ign.ku.dk)

Abstract

Estimating evaporation is important when managing water resources and cultivating crops. Evaporation can be estimated using land surface heat flux models and remotely sensed land surface temperatures (LST), which have recently become obtainable in very high resolution using light weight thermal cameras and Unmanned Aerial Vehicles (UAVs). In this study a thermal camera is mounted on a UAV and applied into the field of heat fluxes and hydrology by concatenating thermal images into mosaics of LST and using these as input for the two source energy balance modelling scheme (TSEB). Thermal images are obtained with a fixed-wing UAV overflying a barley field in western Denmark during the growing season of 2014 and a spatial resolution of 0.20 m is obtained in final LST-mosaics. Two models are used: the original TSEB model (TSEB-PT) and a dual-temperature-difference model (DTD). In contrast to the TSEB-PT model, the DTD model account for the bias that is likely present in remotely sensed LST. TSEB-PT and DTD have been well tested, however only during sunny weather conditions and with satellite images serving as thermal input. The aim is to assess whether a lightweight thermal camera mounted on a UAV is able to provide data of sufficient quality to constitute as model input and thus attain accurate and high spatial and temporal resolution surface energy heat fluxes, with special focus on latent heat flux (evaporation). Furthermore, this study evaluates the performance of the two source energy balance scheme during cloudy and overcast weather conditions, which is feasible due to the low data retrieval altitude (due to low UAV flying altitude) compared to satellite thermal data that are only available during clear sky conditions. TSEB-PT and DTD fluxes are compared and validated against eddy covariance measurements and the comparison show that both TSEB-PT and DTD simulations are in good agreement with eddy covariance measurements with DTD obtaining the best results. The DTD model provides results comparable to studies estimating evaporation

with similar experimental setups, but with LST retrieved from satellites instead of a UAV. Further, systematic irrigation patterns on the barley field provide confidence to the veracity of the spatially distributed evaporation revealed by model output maps. Lastly, this study outlines and discusses the thermal UAV image processing that result in mosaics suited for model input. This study shows that the UAV platform and the lightweight thermal camera provide high spatial and temporal resolution data valid for model input and for other potential applications requiring high resolution and consistent LST.

Comment [HHMN1]: Abstract has been re-written.

1 Introduction

Evaporation (latent heat flux) serves as a key component in both hydrological and land-surface energy processes. However, it is often estimated indirectly because spatially distributed, physical measurements of evaporated water are cumbersome. Provided information on net solar radiation (R_n), sensible- (H) and soil heat flux (G), the latent heat flux (LE) can be estimated as a residual using the assumption of surface energy balance in cases with no significant heat advection:

$$R_n = H + \mathrm{LE} + G \quad (1)$$

All terms in the above equation are related to the land surface temperature (LST). Since the 1980s estimates of evaporation have been obtained through remotely sensed LST and advanced land surface heat flux models accounting for vegetation, soil and atmospheric conditions (Anderson et al., 1997; Kalma et al., 2008) and a large number of heat flux models exist with significant variations in physical system conceptualisation and input requirements (Boulet et al., 2012; Kustas and Norman, 1996; Stisen et al., 2008). Norman et al. (1995) applied the two source energy balance model (TSEB) (Shuttleworth and Wallace, 1985) to remotely sensed data and this modelling scheme has proven to estimate reliable surface heat fluxes over cropland, rangeland and forest at various spatial scales (Anderson et al., 2004; Norman et al., 2003). The TSEB modelling scheme generates robust estimates of surface heat fluxes despite a simple solution scheme demanding relatively few input data. It was developed to be operational using thermal satellite images (Anderson et al., 2011) which serves as a key boundary condition in simulations. The TSEB modelling scheme partitions the remotely sensed LST into two layers; a soil temperature and a canopy temperature, using a Priestley-Taylor approximation (Priestley and Taylor, 1972). This enables a partition of heat flux estimations into its components from soil and canopy respectively. This approach is hereafter referred to as TSEB-PT in order to differentiate it from other TSEB approaches, such as TSEB-LUE (Houborg et al., 2012), based on the Light Use Efficiency concept, or TSEB-2ART, which utilizes dual angle LST observations for direct retrieval of soil and canopy temperatures (Guzinski et al., 2015).

Remotely sensed LST may deviate from the actual surface temperature by several degrees Kelvin due to atmospheric and surface emissivity effects. Consequently thermal-based models utilizing remotely sensed LST that do not address this issue are prone to producing less accurate results. Trying to overcome this issue, Norman et al. (2000) developed the Dual-Temperature-Difference model (DTD) by incorporating two temperature observations into the TSEB modelling scheme; one conducted an hour after sunrise and another conducted later the same day when flux estimations are desired. One hour after sunrise, the surface heat fluxes are neglectable and observations acquired at this time represent a 'starting point' for the temperatures collected later the same day. For agricultural and some hydrological purposes, there is a shortcoming in spatial and temporal resolution of satellite observations (Guzinski et al., 2014). This is

especially true in areas where overcast weather conditions often occur, such as in northern Europe where the present study is conducted, as satellite thermal infrared and visible observations cannot penetrate clouds (Guzinski et al., 2013). Unmanned aerial vehicles (UAVs) (or Remotely Piloted Aircraft System, RPAS, in its most recent terminology) enable a critical improvement for spatial and temporal resolution of remotely sensed data. UAVs can operate at any specific time of day and year provided that strong wind and rainfall are absent. The relative low flying height enable both data collection during overcast conditions (Hunt Jr et al., 2005) and data with higher spatial resolution than what can be obtained from satellite data. Here we hypothesis that UAV data can substitute satellite images and in combination with the presented heat flux models, can be used to generate spatially detailed heat flux maps that provide insight to different evaporation rates and plant stress at decimeter scale. There is rapidly growing interest in the potential of data collection with UAVs, particularly in the science of precision agriculture but also in a range of different scientific and commercial communities (Díaz-Varela et al., 2015; Gonzalez-Dugo et al., 2014; Swain et al., 2010; Zarco-Tejada et al., 2013, 2014). As scientists strive to understand the potential of UAVs and the new applications to which they are suited, the development of efficient workflows, operational systems and improved software that capture and process UAV data are continuing (Harwin and Lucieer, 2012; Lucieer et al., 2014; Turner et al., 2012; Wallace et al., 2012). However, research in possibilities and limitations of UAV platforms is still at an early stage and the present paper introduces the usage of UAV platforms into the fields of heat fluxes and hydrology.

In this study, surface energy balance components are estimated using LST retrieved with a UAV and used as input for the physically-based, two source energy balance models: TSEB-PT and DTD. The aim is to assess whether a lightweight thermal camera installed on board a UAV is able to provide data of sufficient quality to attain high spatial and temporal resolution surface energy heat fluxes. Besides facilitating high resolution LST, the UAV platform enable the application of TSEB-PT and DTD models in cloudy and overcast weather conditions. Model outputs are quantitatively validated with data from an eddy covariance system located at the same barley field over which the UAV flights were conducted and known irrigation patterns provide confidence to the spatially distributed evaporation variations revealed within the barley field. Additionally, this study outline thermal UAV image processing which result in mosaics suited for model input.

2 Materials and methods

Comment [HHMN2]: The method description has been re-structured and ‚Materials and methods' now include site-, data collection- and model descriptions.

2.1 Site

The TSEB models are applied in the HOBE (Hydrological OBsErvatory) agricultural site within the Skjern River catchment, western Denmark, see Fig. 1. The 400 x 400 m site is located in the maritime climate zone where mild winters and cold summers result in a mean annual temperature of 8.2˚C and a mean annual precipitation of 990 mm. The prevailing winds are westerly and windy conditions are common; with 30% of wind in 2014 coming from westerly direction and an average wind speed of 3.8 ms^{-1}. Cloudy and overcast weather conditions are frequent with 1727 hours of sunshine in 2014, which is 16% above normal (Cappelen, 2015). The site is cultivated with barley during UAV campaign and a plow layer of homogeneous sandy loam soil constitutes the upper layer of the soil profile. Course sand is found from 0.25 m and downwards. Soil porosity of the upper 1 m range between 0.35 and 0.40 and the available soil water [pF

2.0–4.2, suction pF = $\log_{10}$(suction in centimeters of water)] is 19% (v_{water}/v_{soil}) in the upper 0.20 m of the plow layer and only 6% (v_{water}/v_{soil}) in the remaining part of the root zone, necessitating frequent irrigation to maintain crop growth during growing seasons (Ringgaard et al., 2011). The overall area is somewhat heterogeneous consisting of three barley fields separated by a gravel road to the south and a row of conifers to the west. Conifers are bordering the barley fields at several places. A meteorological tower with an eddy covariance system consisting of a Gill R3-50 sonic anemometer and a LI-7500 open path infrared gas analyser, is located in the middle of the site (black square in Fig. 1). Meteorological data used as input to the models and as heat flux-validation are measured at this tower.

Comment [HHMN3]: Description of soil properties is expanded and wind conditions are quantitatively described.

2.2 UAV campaign

UAV data was collected on seven days distributed evenly during spring and summer 2014 (Table 1). In total 19 flights were conducted, of which 7 were flown early in the morning, constituting the additional input data for the DTD model. The entire airborne campaign thus resulted in 12 sets of input data for the TSEB-PT and DTD model. Dates with (c) in Table 1 mark days where the UAV flights were conducted in cloudy or overcast conditions.

A fixed-wing UAV (Q300, QuestUAV, UK) with a wingspan of 2.2 m was used as platform for the airborne operations. It was able to carry a payload of 2 kg for approximately 25 min in the air. With a speed of 60 km h^{-1} and flying height of 90 m above ground, the 400×400 m site area was covered in a single flight. The UAV was controlled by the SkyCircuits Ltd SC2 autopilot in a dual redundant system with separate laptop and transmitter control. Communication between autopilot and ground was performed by a radio link that transmits position and attitude. Landing was conducted manually using the transmitter. SkyCircuits Ground Control Station software was used for generating the flight route and for visual inspection of the UAV, while it was is in the air.

2.3 Thermal data and image processing

An Optris PI 450 LightWeight infrared camera of 380 g was mounted on the UAV. The camera detects infrared energy in the 7.5-13 µm thermal spectrum and surface temperatures were computed automatically using a fixed emissivity of unity. Thermal images were stored at 16 bit radiometric resolution. According to manufacturer specifications, the system has an accuracy of +/- 2°C or +/- 2% at an ambient temperature of 23+/-5 °C. The thermal detector within the camera collects an image array of 382×288 pixels with a nadir viewing footprint of 50×40 m per image at 90 m flying height, resulting in an effective ground resolution of approx. 0.13 m per pixel.

Time synchronization between camera and autopilot was necessary in order to link the logged GPS and rotation position with each image. This was performed before launching the UAV with a USB GPS connected to the camera thus synchronizing the timestamp on each image with the GPS clock. Timestamps were recorded in UTC time and accurate to within 1 second. Re-calculation of camera position was therefore necessary and performed using a self-calibrating bundle adjustment in Agisoft PhotoScan software (Professional Edition version 1.0.4). No ground control points were used, nor needed, during camera alignment and bundle adjustment. Images were converted into unsigned 16 bit data to enable processing in Photoscan.

Between 700 and 1000 images were collected for each flight with camera recording in continuous mode, triggering an image every second. Generally half of the images were suitable for further processing. Non-suitable images occur due to strong gusts of wind affecting flight velocity which causes poor quality recording and blurry images. Images collected during take-off and landing were likewise discarded before post-processing. In addition to re-calculating the camera positions, the self-calibrating bundle adjustment computed three dimensional point clouds from which thermal ortho-mosaics were built using a mean value composition. The view zenith angle of ortho-mosaics was set to 0° for all pixels, hence the largest possible amount of soil was assumed visible.

The thermal mosaics served as key boundary conditions to TSEB-PT and DTD. Resulting resolution on thermal mosaics from midday flights was 0.20 m. However, the software was not able to mosaic the early morning data, presumably because temperatures were too homogeneous to enable the detection of common features between images needed for the bundle adjustment. Consequently, LST from early morning flights were extracted manually and only the average LST for the barley fields was used as the additional data input for DTD model runs. This average was a satisfying representation of sunrise LST because of its homogenous nature.

2.4 Heat flux models

The original TSEB model developed by Norman et al. (1995) is a two-layer model of turbulent heat exchange. Observations of remotely sensed LST are split into two layers: a canopy (T_C) and a soil (T_S) temperature. This is performed with the Priestley-Taylor approximation that partitions the divergence of net radiation in the canopy into sensible and latent heat fluxes. The initial estimate of canopy sensible heat flux is used to split LST into canopy and soil temperatures, enabling separation of sensible and latent heat flux between canopy and soil. Further it enables a simpler parameterisation of resistances compared to single layer models (Monteith, 1965) as no empirical excess resistance adjustment is needed for the calculation of the bulk sensible heat flux (Norman et al. 1995). The excess resistance term is used in single-layer models in order to correct for a substitution of directional radiometric temperature for aerodynamic temperature when calculating sensible heat fluxes (Eq. 5, 8 and 9 in Norman et al. (1995)). The TSEB modelling scheme uses directional radiometric temperature (collected with the thermal camera and UAV) and therefore no substitution of temperatures or correction via the excess resistance is needed. Section 2.2.1 and 2.2.2 contain equations of relevance for the present study and highlight the difference between TSEB-PT and DTD computations.

2.4.1 TSEB-PT

Net radiation (R_n) and the three resistances in this soil-canopy-atmosphere heat flux network: the aerodynamic resistance to heat transfer (R_A), the resistance to heat transport from soil surface (R_S) and the total boundary layer resistance of leaf canopy (R_X) (all in s m^{-1}) remain constant during the individual model runs. For calculations of R_A and R_S, see Norman et al. (2000) Eq. 10 and 11, for calculations on R_X see Norman et al. (1995) Eq. A8.
R_n is calculated as a sum of short- and long wave radiation:

$$R_n = \left(R_{s,in} - R_{s,out}\right) + \left(R_{l,in} - R_{l,out}\right) \quad (2)$$

$$R_{s,in} - R_{s,out} = R_{s,in}(1 - \alpha) \quad (3)$$

$$R_{l,in} - R_{l,out} = \epsilon_{surf}\epsilon_{atm}\sigma T_A^4 - \epsilon_{surf}\sigma T(\theta)_R^4) \quad (4)$$

where R_s, R_l is short- and long wave radiation respectively and $_{in}$ and $_{out}$ refers to the direction of the radiation, α is the combined vegetation and soil albedo which was estimated from incoming and outgoing short wave radiation from a four-component radiation sensor (NR01, Hukseflux Thermal Sensor). Albedo for bare soil was measured before the first barley shouts appeared on the surface and was kept fixed (although some changes are expected with soil humidity) whereas albedo for vegetation was retrieved for each flying day and hence varied between individual model runs. Combined vegetation and soil albedo for each flying day is shown in Table 2. σ is Stefan-Boltzman constant, T_A is air temperature (K) attained from the meteorological tower (section 2.1), $T(\vartheta)_R$ is radiometric land surface temperature (K) which in the present study is collected with a UAV. ϵ_{surf} is combined vegetation and soil emissivity obtained under similar conditions from Guzinski et al. (2014) and ϵ_{atm} is atmosphere emissivity computed as in Brutsaert (1975):

$$\epsilon_{\text{atm}} = 1.24(\frac{ea}{T_A})^{0.14286} \quad (5)$$

where e_a is water vapor pressure (mb) attained from meteorological tower.

Assuming neutral atmospheric stability and the Monin-Obukhov length tending to infinity, the iterative part of the model is then initiated.

During first iteration the net radiation divergence, partitioning R_n into radiation reaching the soil ($R_{n,S}$) and the canopy ($R_{n,C}$) respectively, is computed as in (Norman et al., 2000):

$$\Delta R_n = R_n\left[1 - \exp(\frac{-\kappa F\Omega_0}{\sqrt{2\cos(\theta_s)}})\right] \quad (6)$$

Where Ω_0 is the nadir view clumping factor that depends on the ratio of vegetation height to plant crown width which is set to 1.0, ϑ_s is the sun zenith angle calculated by model from time of the day, κ is an extinction coefficient varying smoothly from 0.45 for LAI more than 2 to 0.8 for LAI less than 2, and F is the total Leaf Area Index (LAI). Measurements of LAI were obtained with a canopy analyzer LAI2000 instrument three times during the UAV campaign: 21 May 2014, 3 June 2014 and 18 June 2014 and an average from six locations in the northern and southern barley fields were computed for each day. LAI values for each model run were extrapolated from these measurements taking canopy height and fraction of green vegetation into account.

Sensible heat flux of the canopy can thus be estimated using the Priestley-Taylor approximation:

$$H_C = \Delta R_n\left(1 - \alpha_{PT} f_g \frac{sp}{sp+\gamma}\right) \quad (7)$$

Where α_{PT} is the Priestley-Taylor parameter set to an initial value of 1.26 assuming unstressed vegetation transpiration (Priestley and Taylor, 1972), f_g is fraction of vegetation that is green which was estimated *in situ* for each flying day (Table 2), sp is the slope of saturation pressure curve and γ is the psychometric constant, both obtained from Allen et al. (1998).

Using the sensible heat flux from canopy, canopy temperature (T_C) can be computed using Eq. A7, A11, A12 and A13 from Norman et al. (1995). Calculations of soil temperature (T_S) can thus be performed:

$$T_S = \left(\frac{T_R^4 - f_\theta T_C^4}{1 - f_\theta}\right)^{0.25} \quad (8)$$

Where f_ϑ is fraction of view of radiometer covered by vegetation calculated as $f_\theta = 1 - \exp(\frac{-0.5\Omega_\theta F}{\cos(\theta)})$, where Ω_ϑ is the clumping factor at view zenith angle (ϑ).

With known resistances and temperatures, fluxes are then calculated in the following sequence (all in W m^{-2}):

$$H_C = \rho c_p \frac{T_C - T_{AC}}{R_X} \quad (9)$$

Where H_C is sensible heat flux from canopy, ρ is air density (kg m^{-3}), c_p is specific heat of air (J kg^{-1} K^{-1}) and T_{AC} is inter-canopy air temperature (K) computed with T_A, T_S, T_C, and resistances.

Canopy latent heat flux:

$$\mathrm{LE_C} = \Delta R_n - H_C \quad (10)$$

Sensible heat flux from soil:

$$H_S = \rho c_p \frac{T_S - T_{AC}}{R_S} \quad (11)$$

Soil heat flux is computed following Liebethal and Foken (2007):

$$G = 0.3R_{n,s} - 35 \quad (12)$$

Comment [HHMN4]: G equations are provided.

Where $R_{n,S}$ is net radiation that reaches the soil surface computed as $R_{n,S} = R_n - \Delta R_n$.

$$\mathrm{LE_S} = R_{n,S} - G - H_S \quad (13)$$

Now it is possible to calculate the total sensible (H) and latent heat fluxe (LE) as a summation of their canopy and soil components: $H = H_C + H_S$ and $\mathrm{LE} = \mathrm{LE_C} + \mathrm{LE_S}$.

The Monin-Obukhov length is then re-calculated according to Brutsaert (2005) Eq. 2.46 and the iterative part of the model is re-run until the Monin-Obukhov length converges to a stable value, at which point the final flux values are attained.

2.4.2 DTD

The DTD model described in Norman et al. (2000) is a further development of the TSEB-PT model. DTD similarly divides the observed LST into vegetation and soil temperatures and computes surface energy balance components following virtually the same procedure. However, DTD accounts for the discrepancy between the fact that the TSEB modelling scheme is sensitive to the temperature difference between land surface and air, and that absolute LST retrieved from remote sensing data are regarded as inaccurate. This is accounted for by adding an additional input dataset: LST retrieved one hour after sunrise when energy

fluxes are minimal. The modelled fluxes are hence based on a temperature difference between the two observations, which is assumed to be a more robust parameter compared to a single retrieval of remotely sensed temperature as it minimizes consistent bias in the temperature estimates. The essential equation that differs between TSEB-PT and DTD is the one computing sensible heat flux. In the series implementation of DTD the linear approximation of Eq. (2) is taken together with Eq. (7) to (9) and applied at midday and one hour after sunrise and subsequently subtracted from each other to arrive at the following:

$$H_i = \rho c_p \left[\frac{(T_{R,i}(\theta_i) - T_{R,0}(\theta_0)) - (T_{A,i} - T_{A,0})}{(1 - f(\theta_i))R_{S,i} + R_{A,i}}\right] + H_{C,i}\left[\frac{(1 - f(\theta_i))R_{S,i} - f(\theta_i)R_{X,i}}{(1 - f(\theta_i))R_{S,i} + R_{A,i}}\right] \quad (14)$$

where subscripts *i* and *0* refer to observations at midday and one hour after sunrise respectively. Since the early morning (time 0) sensible heat fluxes are negligible they are omitted in the above equation.

Computations of soil heat flux (*G*) also differ because the difference in radiometric temperature between sunrise and midday observations can be used as an approximation of the diurnal variation in soil surface temperature. Soil heat flux computations are derived from the soil heat flux model of Santanello and Friedl (2003):

$$G = R_{n,S} A \cos\left(2\pi \frac{t + 10800}{B}\right) \quad (15)$$

Where *t* is time in seconds between the observation time and solar noon, $A = 0.0074\Delta T_R + 0.088$, $B = 1729\Delta T_R + 65013$ and ΔT_R is an approximation of the diurnal variation in the soil surface temperature from UAV data.

For an in-depth review of the TSEB-PT and DTD models including all equations, see Guzinski et al., (2014) and Guzinski et al. (2015).

2.5 Footprint extraction from model output maps

In order to compare modelled R_n, *H, G* and LE to measurements from the eddy covariance system, a single representative value from each TSEB-PT and DTD output map has to be extracted in accordance with the coverage of eddy covariance footprints. Each eddy flux measurement represents an area for which the size, shape and location are determined by surface roughness, atmospheric thermal stability and wind direction at a given time – in this case UAV flight times. Sensible and latent heat fluxes are extracted from TSEB-PT and DTD maps using a two-dimensional footprint analysis approach as described in Detto et al. (2006). The twelve footprint outputs were applied to corresponding maps of sensible and latent heat fluxes by weighing each modelled pixel according to the contribution of that pixel's location to the measured flux. Approximations of the 70 % eddy flux footprint-coverages are shown in Appendix B. Net radiation and soil heat flux measurements have footprints that are much smaller than sensible and latent heat flux measurements and values from *R*n and *G* output maps were extracted from a 5×5 m area on the barley field next to the eddy flux tower.

Comment [HHMN5]: Description of the TSEB modelling scheme has been re-structured and re-written.
Referee # 1 and #2 were divided regarding the degree of details that the model description had to include. We have chosen not to present all equations in the TSEB modelling scheme as this has been done in several other papers and only present the equations of relevance for this specific purpose: Illustrating that temperatures collected with a UAV can serve as boundary condition when estimating heat fluxes with the TSEB modelling scheme. We think the revised model description gives a better overview because it is structured in the sequence the equations are executed during simulations. Further it should provide a better understanding of how field observations are applied in the models.

2.6 Validation data

An eddy covariance system consisting of a Gill R3-50 sonic anemometer and a LI-7500 open path infrared gas analyzer was mounted 6 m above ground in the middle of the site (see Fig. 1). Wind components in three dimensions and concentrations of water vapor were measured at 10 Hz. Sensible and latent heat fluxes for validation of model outputs were computed from the eddy covariance system using EddyPro 5.1.1 software (Fratini and Mauder, 2014). Computations include two dimensional coordinate rotation, block averaging of measurements in 30 min windows, corrections for density fluctuations (Webb et al., 1980), spectral corrections (Moncrieff et al., 2005; Moncrieff, J B et al., 1997) and measurement quality checking according to Mauder and Foken (2006). Furthermore, the computed heat fluxes were subject to an outlier quality control following procedures described in Papale et al. (2006). Short- and long wave, incoming and outgoing radiation and soil heat fluxes were measured with a Hukseflux four component net radiometer (model NR01) and heat flux plate (model HFP01). Gap-filling of the validation data was not required because no gaps in the data occurred during the twelve flights. When applying the surface energy balance expression any residual was assigned to latent heat flux, as recommended by Foken et al. (2011). This ensures energy balance closure and comparability with TSEB-PT and DTD modelled fluxes. The average-size of residuals from the twelve datasets was 9 %.

3 Results and discussion

TSEB-PT and DTD models are executed twelve times with data collected on seven days during the spring and summer of 2014. Spatially distributed maps of net radiation, soil-, sensible- and latent heat fluxes are attained with resolutions of 0.20 m.

3.1 Comparison between fluxes from UAV data and eddy covariance

Modelled fluxes attained with thermal UAV data and measured fluxes from the eddy covariance system are shown in Table 3. As expected, there are large variations throughout the season determined primarily by time of year and time of day – dates and hours with potentially large incoming solar radiation (summer and midday) contain potential for largest evaporation. Figure 2A-C show modelled versus measured fluxes and a statistical comparison is presented in Table 4. Calculations for R_n are alike in TSEB-PT and DTD and generally in good agreement with measured R_n with a RMSE value of 44 W m^{-2} (11 %) and a correlation coefficient (r) of 0.98 (Table 4). Simulated R_n from 10 April and 2 July 2014 are in less good agreement with measured R_n and are underestimated with 88 W m^{-2} and 96 W m^{-2} respectively. Modelled R_n consists of short- and longwave incoming and outgoing radiation ($R_{s,in}$, $R_{s,out}$, $R_{l,in}$, $R_{l,out}$) of which $R_{s,in}$ is provided as model input from eddy tower measurements. This contributes positively to the agreement between modelled and measured R_n but it cannot be assigned to model performance or the quality of collected temperature data. Therefore a comparison is also conducted between modelled and measured net longwave radiation (R_l), which as opposed to modelled and measured R_n, are entirely independent of each other. The TSEB modelling scheme produce R_l estimates to a satisfactory level if results from 10 April and 2 July are not regarded, see appendix A. R_l estimates depend on atmospheric emissivity which in the TSEB modelling scheme are calculated with Eq. 5 (from Brutsaert (1975)). Eq. 5 builds on the assumption of exponential atmospheric profiles for temperature, pressure and humidity. The stability of atmosphere is

affected by relative humidity (RH) (Herrero and Polo, 2012) and errors between measured and modelled R_l are related to RH in second graph in appendix A. It is seen that there's a correlation between the highest errors and the highest RH. This suggests that assumptions behind Eq. 5 might not be met on 10 April and 2 July. Different approaches for estimating R_l could have been chosen for these two dates (e.g. Brutsaert (1982)) but for simplicity the approach presented in Brutsaert (1975) is maintained for all dates. Appendix A show that if algorithm-assumptions are met, UAV collected surface temperatures can be satisfactorily used to estimate R_l using the TSEB scheme. Eq. 5 also builds on the assumption of clear skies. Since poor simulations of R_l is not significant in data collected in overcast conditions, the larger incoming longwave radiation due to clouds might compensate for the smaller path between UAV and surface, compared to between satellite and surface.

Comment [HHMN6]: Comparison between measured and modelled net longwave radiation is included and effects of atmospheric emissivity discussed.

Sensible heat fluxes (*H*) are generally well estimated by both models. TSEB-PT sensible heat fluxes are consistently underestimated, however r is better (in contrast to RMSE and MAE) than r calculated for DTD. This implies a better linear relation between measured and modelled sensible heat flux from TSEB-PT, see Fig. 2B. The DTD model computes slightly more scattered sensible heat fluxes but results do not show any systematic errors – they are centered around measured values and are generally in better accordance with measured fluxes with RMSE and MAE values of 59 W m^{-2} (64 %) and 49 W m^{-2} (52 %), compared to TSEB-PT RMSE and MAE values of 85 W m^{-2} (91 %) and 75 W m^{-2} (81 %).

Soil heat fluxes (*G*) are generally underestimated by both algorithms and RMSE and MAE values of 48 W m^{-2} (91 %) and 45 W m^{-2} (86 %), and 38 W m^{-2} (72 %) and 35 W m^{-2} (66 %) are obtained from DTD and TSEB-PT respectively. *G* was measured from two heat flux plates located approximately 3 cm below the surface. Heat flux plates might not provide the best estimate of energy partitioning at the surface (Jansen et al., 2011) which could lead to uncertainties in measured *G*. Further, the difference between heat conduction of soil and air create a discrepancy between measured *G* and *H* and LE, since fast changes in *R*n (as a consequence of intermittent cloud cover) will have a faster response in *H* and LE than in *G* (Gentine et al., 2012). The TSEB modelling scheme does not account for the delay in G response and therefore also a discrepancy between measured and modelled *G* will occur. However the magnitude of *G* is small compared to the remaining surface energy fluxes and therefore has a comparably small impact on LE estimations even though it is computed as a residual of R_n, *H* and *G*.

Comment [HHMN7]: Measured and modelled G are presented and results are discussed concerning consequences of intermittent cloud cover.

Modelled latent heat flux (LE) is in good agreement with measured latent heat fluxes. As a consequence of underestimation of sensible heat flux in TSEB-PT simulations, a small overestimation of TSEB-PT latent heat flux is seen (Fig. 2C). DTD latent heat flux is again more scattered but with lower RMSE and MAE values of 67 W m^{-2} (26 %) and 57 W m^{-2} (22 %), compared to TSEB-PT RMSE and MAE values of 94 W m^{-2} (37 %) and 84 W m^{-2} (33 %).

The DTD algorithm generally produces results in better accordance with measurements and is concluded to be a better algorithm when simulating heat fluxes with present experimental setup. This suggests a consistent bias in the UAV derived LST which can be corrected by subtracting the early morning observations from the midday ones and demonstrates the robustness and added utility of the DTD approach. A calibration of the camera with in situ temperatures would likely have improved TSEB-PT heat flux computations. Further a conversion of brightness temperature to actual LST using a spatially distributed emissivity would presumably improve both TSEB-PT and DTD results. In average there was a 95 % overlap between the coverage of eddy flux footprints and the model output maps from all twelve

datasets. The lacking percentages of fluxes from maps were simply added from the flux values obtained from overlapping eddy flux footprints and maps. This introduces a small uncertainty to the extraction of flux values from model output and thus also to the comparison between measured and modelled *H* and LE.

Guzinski et al. (2014) applied their TSEB-PT study to the same field site as the present study but they used thermal satellite images from Landsat as boundary conditions as opposed to thermal UAV images. A comparison between the two studies shows similar accurate results. Guzinski et al. (2014) achieve RMSEs of 46 W m^{-2} for R_n, 56 W m^{-2} for *H* and 66 W m^{-2} for LE (Table 2, column ND_H in Guzinski et al. (2014)). This study achieves RMSEs of 44 W m^{-2} for R_n, 59 W m^{-2} for *H* and 67 W m^{-2} for LE, using the DTD model. r is likewise similar between the two studies. However, when Guzinski et al. (2014) uses both MODIS and Landsat data to disaggregate DTD fluxes, modelled sensible and latent heat fluxes were in better agreement with the observed fluxes (Table 2, column EF in Guzinski et al. (2014)). Further, a comparison between this study and other studies seeking to estimate surface fluxes from remotely sensed data (such as Colaizzi et al. (2012); Guzinski et al. (2013); Norman et al. (2000)) show that measured and modelled fluxes are in same order of agreement.

Contrary to studies using satellite images, the majority of data in this study is retrieved under cloudy or overcast conditions. Data collected during sunny conditions are enclosed by black circles in Fig. 2A-C and Table 5 shows statistical parameters calculated using only data from days with cloudy or overcast weather conditions. Based on Fig. 2A-C and on a comparison between statistical parameters in Table 4 and 5, no significant difference can be seen between data collected during cloudy, overcast and sunny weather conditions. Thus it is concluded that the TSEB modelling scheme can be applied to data obtained in all three weather types. However, it is worth mentioning that data collected during conditions with scattered clouds, and hence quickly changing irradiance, would lead to large variations in retrieved LST during a single flight. LST collected with UAVs are instantaneous but also a mosaic of instantaneous LST collected in a time span of 20 min. Comparing this kind of measurement to a 30 min flux average from the eddy covariance system can lead to disagreement between measured and modelled fluxes (Kustas et al., 2002).

The view zenith angle of ortho-mosaics was set to 0° (section 2.3). However the maximum view zenith angle of the thermal camera is 15° and setting a theoretical view zenith angle to 0° could lead to a small overestimation of latent heat flux. Any bias due to the 0° view zenith angle in models could maybe have been accommodated using a maximum value composition (instead of a mean value composition) when generating LST-mosaics. However, a mean value composition was used because the mosaics produced with this method compared well with mosaics produced manually in which the edges of each image were removed. Edges were removed in order to eliminate the vignetting effect, which generally affects thermal images in particular and therefore also the images collected in this study. Using a mean value composition is thus assumed to enable the usage of entire images without eliminating or correcting for vignetting effects. Using entire images allow a larger image overlap which is crucial when images are mosaicked in Photoscan. The difference between using a mean and a maximum value composition was approx. 0.3° Kelvin and 5 W m^{-2} latent heat flux for mosaic from 10 April 2014.

Disagreement between measured and modelled fluxes may also be due to the presented approach of handling the residual between eddy covariance surface energy fluxes. The average-size of residuals from the twelve datasets was as mentioned 9 % (section 2.6). A different approach to handling the energy

balance residual (e.g Foken, 2008) would lead to slightly different results in the comparison between measured and modelled fluxes.

Comment [HHMN8]: Considerations regarding lack of closure in measured fluxes.

3.2 Spatial patterns in evaporation maps

The TSEB modelling scheme, with input of high spatial resolution temperatures, produce spatially distributed heat flux maps which reveal patterns in the evaporation which could not have been quantified through more established techniques, such as eddy covariance systems or when using satellite data. Twelve evaporation maps computed with DTD are shown in Appendix B. Patterns of evaporation within the barley fields are the same for TSEB-PT and DTD maps. The maps differ in size due to different flight routes, which are determined by wind direction and velocity on the given day. This study does not have access to data with same spatial resolution that could have validated the evaporation patterns. However the irrigation system applied to the barley field constitute valid explanation for patterns seen in maps from the late growing season, which provides confidence on spatial patterns seen in all maps:

During the UAV campaign the barley field was irrigated five times: 23 May, 29 May, 5 June, 15 June and 25 June, 2014. On each occasion 25 mm of water was applied. Irrigation is performed with a traveling irrigation gun that is automatically pulled across the field in tramlines that run in north-south direction on northern field and east-west direction on southern field, Fig. 3. The irrigation tubing has to be moved manually to a new tramline when the distance of one tramline has been traveled and the pattern of which water is irrigated remains the same during entire growing season.

The evaporation maps from 18 June 2014 and onwards (when irrigation would plausible have made its mark on plant health) reveal significant differences within the barley fields: patterns of approx. 20 m wide blueish areas running parallel to the tramlines. The blueish color illustrate that these areas produce less evaporation than the surrounding field. The location of these areas corresponds well with areas where irrigators running in tramline trails have not been able to irrigate as intensively as areas closer to the tramlines (Fig. 3). These areas likely consist of less healthy plants which will generate higher LST and lower rates of evaporation. Recognition of very likely patterns of evaporation within the barley field demonstrates a high degree of confidence in the veracity of the spatially distributed model output.

Comment [HHMN9]: A more elaborate explanation of irrigation system and how it will impact evaporation from the barley field is provided. Further Figure 3 show the tramlines in which irrigation guns are placed and that there is a high degree of coincidence between evaporation patterns and repeated patterns of irrigation

4 Conclusions and outlook

Land surface temperatures (LST) were obtained with a lightweight thermal camera mounted on a UAV with the ability to cover a 400 x 400 m barley field in both sunny, cloudy and overcast weather conditions. Thermal images were successfully concatenated into LST-mosaics that served as key boundary condition to the two source energy balance models: TSEB-PT and DTD. Simulated net radiation, soil-, sensible- and latent heat fluxes were in good agreement with flux measurements from an eddy covariance system located at same barley field at which the UAV flights were conducted, with the DTD simulations showing better agreement with measurements. In contrast to TSEB-PT, the DTD model accounts for the bias in remotely sensed LST, likely to be present in images from the lightweight thermal camera. Systematic irrigation patterns on the barley field support the confidence in the veracity of the spatially distributed evaporation patterns produced by the models. A comparison between present results and results from

other studies estimating surface energy fluxes from heat flux models and remotely sensed LST, reveal that the UAV platform and the lightweight thermal camera provide good quality, high spatial and temporal resolution data that can be used to generate surface energy fluxes with similar accuracy as can be generated using satellite data. LST-mosaics can be used for model input and for other potential applications requiring high resolution and consistent LST. Additionally, the UAV platform accommodated validation of the applicability of the TSEB modelling scheme in cloudy and overcast weather conditions which was possible due to the low altitude retrieval of LST compared to satellite retrievals of LST which are only feasible during clear sky conditions.

Future improvements will incorporate spatially distributed optical data into the two source energy balance models in order to estimate spatially varying ancillary variables such as albedo, leaf area index and canopy height. This will enable flux estimations in areas with heterogeneous vegetation types and have a positive effect on estimations over maturing crops when differences in irrigation may have impacted their developmental stage.

Extending the present setup to other land cover types would further strengthen the applicability of thermal UAV data and presented model scheme. A calibration of the thermal camera with *in situ* temperatures should improve TSEB-PT results with a potential positive effect on DTD results as well.

Adjustments in the TSEB modelling scheme that consider differences between satellite and UAV images might be valuable. The atmospheric path from the ground to satellites and from the ground to UAVs, differs greatly and a comparison between measured and modelled longwave radiation reveal that a different approach for estimating atmospheric emissivity (when using UAV data) might influence results positively.

Appendix A

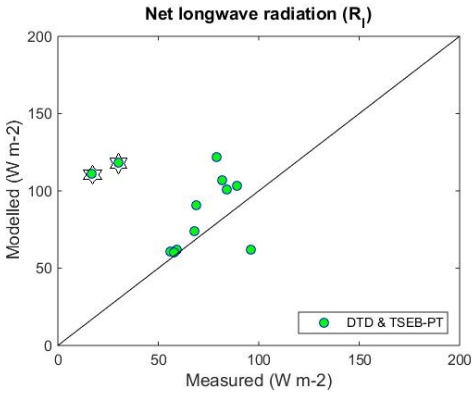

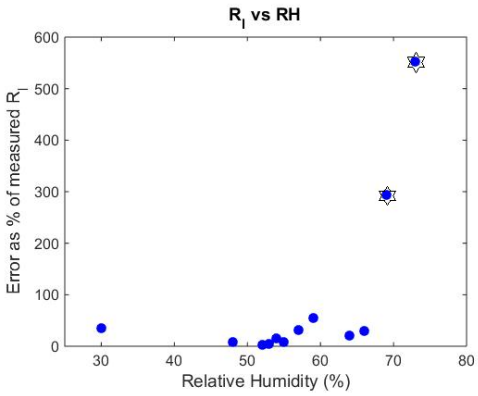

First graph show measured and modelled net longwave radiation (R_l). R_l from 10 April and 2 July 2014 are enclosed by black stars. Second graph show the error between measured and modelled R_l as percent of measured R_l compared to relative humidity at the time of UAV flights. Again measurements from 10 April and 2 July 2014 are enclosed by black stars.

Comment [HHMN10]: Net longwave radiation comparison and investigation of assumptions behind Eq. 5.

Appendix B

Evaporation maps from the DTD model. Black star represent location of eddy flux tower and black circles mark location of eddy covariance footprint.

Comment [HHMN11]: Maps now also illustrate the differences between coverage of EC-footprint for each flight.

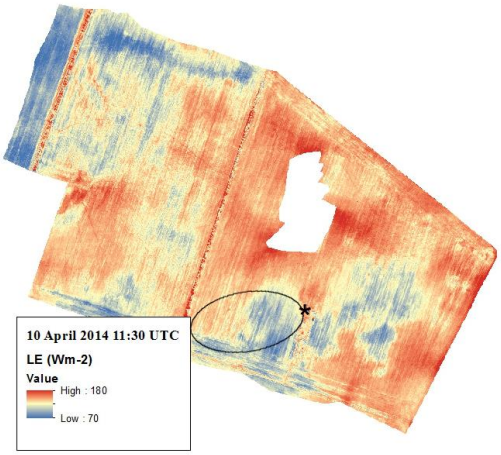

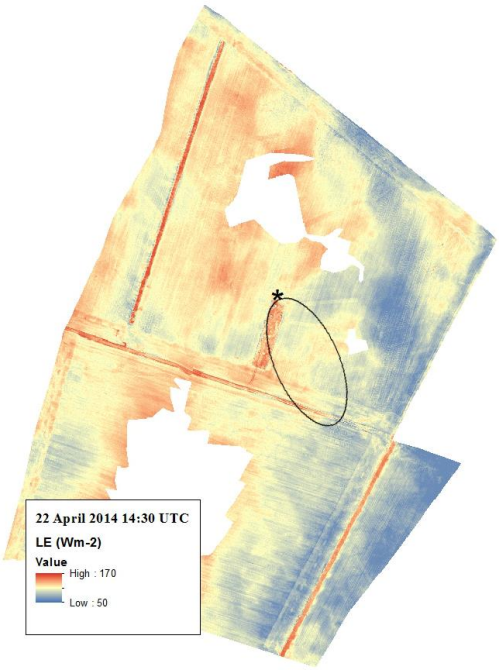

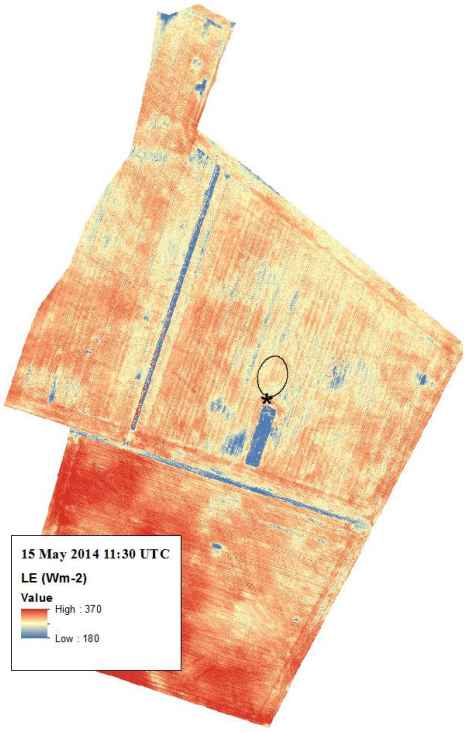

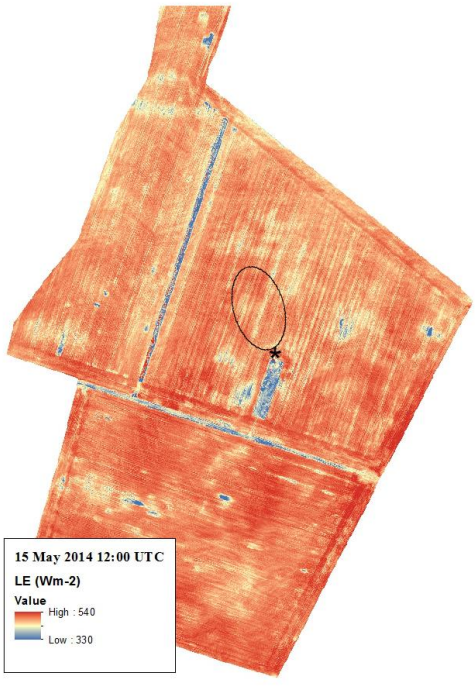

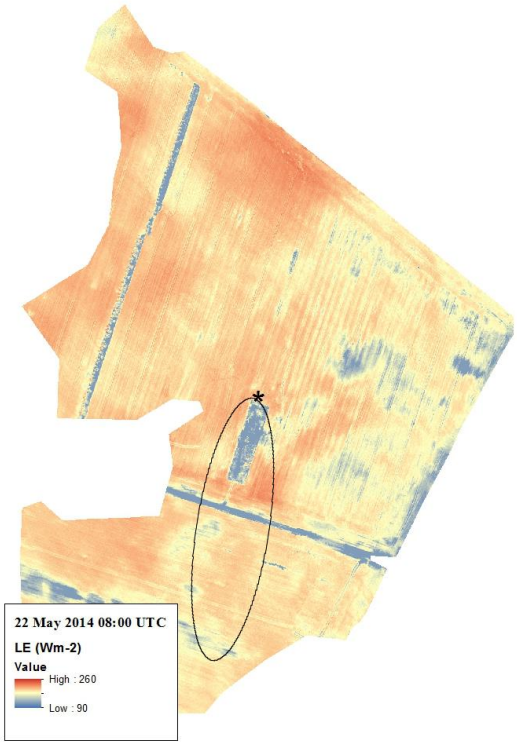
22 May 2014 08:00 UTC
LE (Wm-2)
Value
High : 260
Low : 90

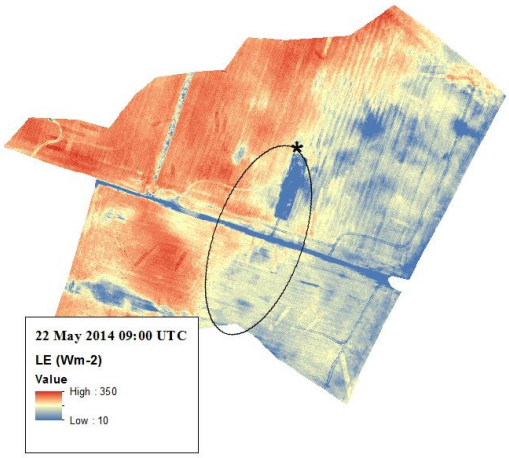
22 May 2014 09:00 UTC
LE (Wm-2)
Value
High : 350
Low : 10

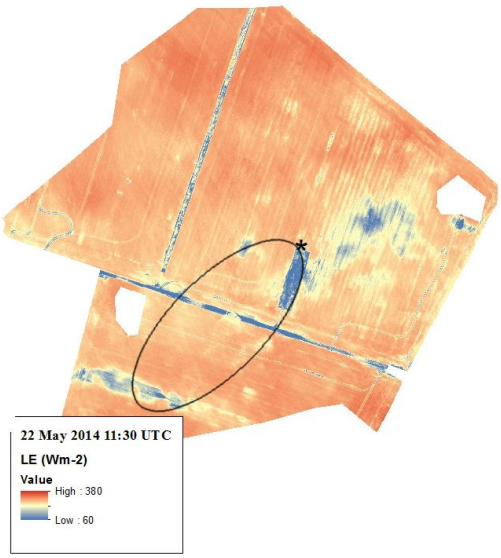
22 May 2014 11:30 UTC
LE (Wm-2)
Value
High : 380
Low : 60

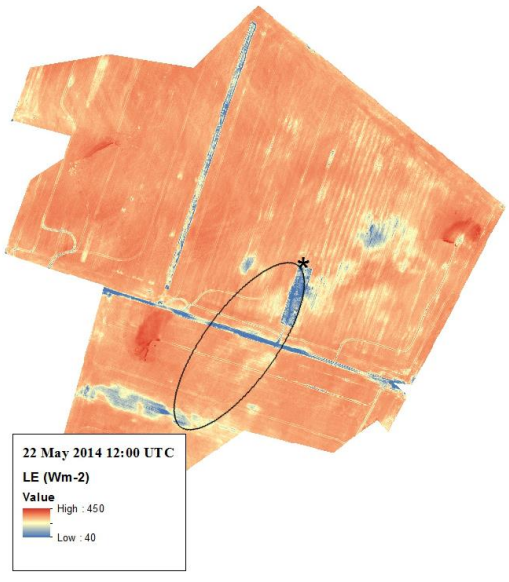
22 May 2014 12:00 UTC
LE (Wm-2)
Value
High : 450
Low : 40

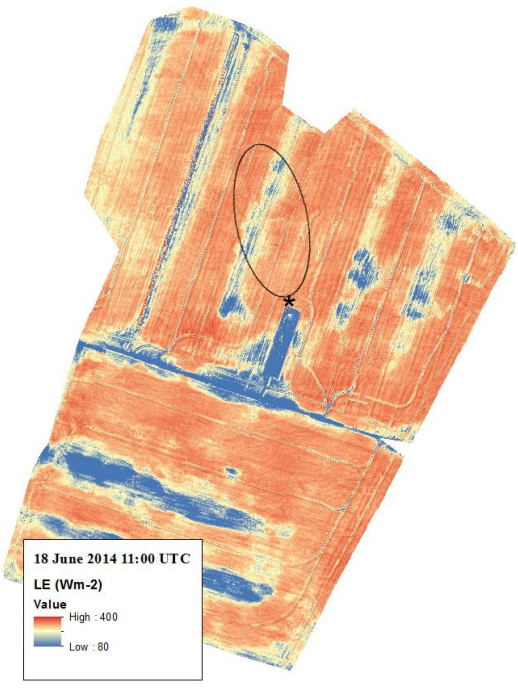
18 June 2014 11:00 UTC
LE (Wm-2)
Value
High : 400
Low : 80

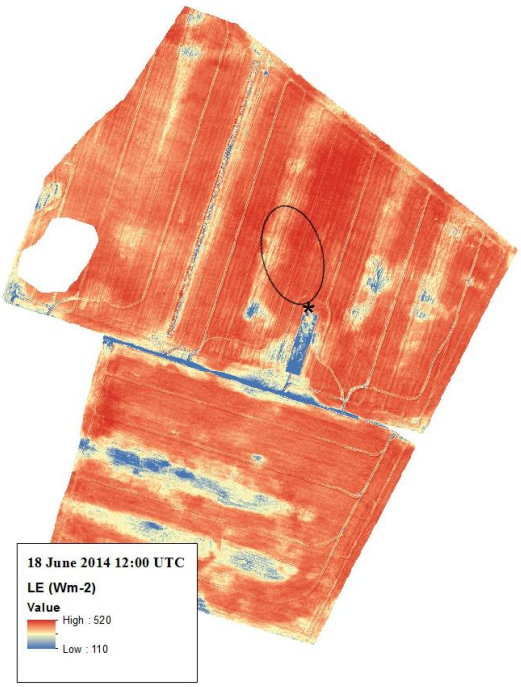
18 June 2014 12:00 UTC
LE (Wm-2)
Value
High : 520
Low : 110

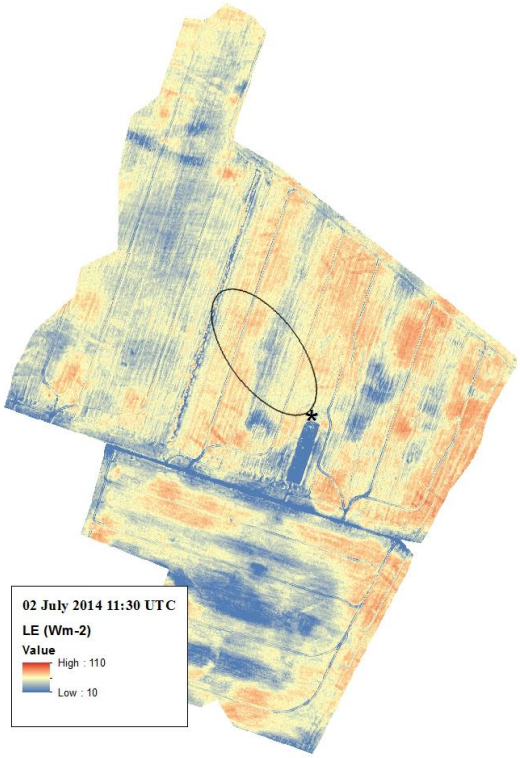
02 July 2014 11:30 UTC
LE (Wm-2)
Value
High : 110
Low : 10

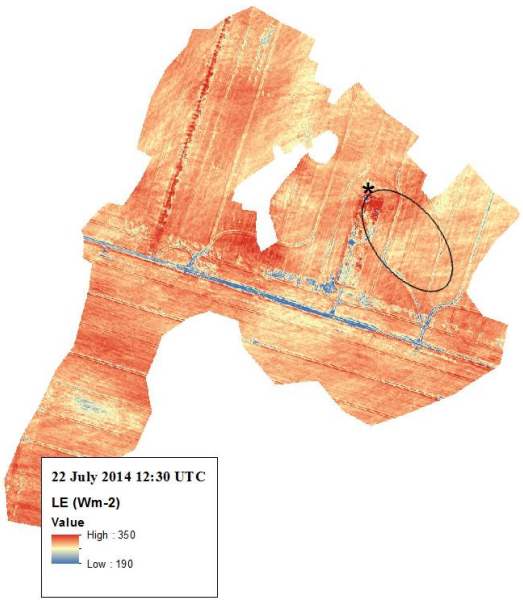
22 July 2014 12:30 UTC
LE (Wm-2)
Value
High : 350
Low : 190

Acknowledgements

This work has been carried out within the HOBE project, funded by the Villum Foundation. Also thanks to Lars Rasmussen and Anton Thomsen for their work in the field that among others ensure flux tower measurements. Further, we are grateful to the Quantalab team at IAS, especially Alberto Hornero Luque, for helping out with thermal camera settings and to Gorka Mendiguren González for providing technical support for footprint applications. Lastly, thanks to Arko Lucieer and his team at University of Tasmania for their willingness to provide general UAV supervision.

References

Allen, R. G., Pereira, L. S., Raes, D., Smith, M. and others: Crop evapotranspiration-Guidelines for computing crop water requirements-FAO Irrigation and drainage paper 56, FAO Rome, 300(9), D05109, 1998.

Anderson, M. C., Norman, J. M., Diak, G. R., Kustas, W. P. and Mecikalski, J. R.: A two-source time-integrated model for estimating surface fluxes using thermal infrared remote sensing, Remote Sens. Environ., 60(2), 195–216, doi:10.1016/S0034-4257(96)00215-5, 1997.

Anderson, M. C., Norman, J. M., Mecikalski, J. R., Torn, R. D., Kustas, W. P. and Basara, J. B.: A multiscale remote sensing model for disaggregating regional fluxes to micrometeorological scales, J. Hydrometeorol., 5(2), 343–363, 2004.

Anderson, M. C., Kustas, W. P., Norman, J. M., Hain, C. R., Mecikalski, J. R., Schultz, L., González-Dugo, M. P., Cammalleri, C., d'Urso, G., Pimstein, A. and Gao, F.: Mapping daily evapotranspiration at field to continental scales using geostationary and polar orbiting satellite imagery, Hydrol. Earth Syst. Sci., 15(1), 223–239, doi:10.5194/hess-15-223-2011, 2011.

Boulet, G., Olioso, A., Ceschia, E., Marloie, O., Coudert, B., Rivalland, V., Chirouze, J. and Chehbouni, G.: An empirical expression to relate aerodynamic and surface temperatures for use within single-source energy balance models, Agric. For. Meteorol., 161, 148–155, doi:10.1016/j.agrformet.2012.03.008, 2012.

Brutsaert, W.: On a derivable formula for long-wave radiation from clear skies, Water Resour. Res., 11(5), 742–744, doi:10.1029/WR011i005p00742, 1975.

Cappelen, J.: Danmarks klima 2014 - with English Summary. DMI Tech. Rep. 15-01. Danish Meteorol. Inst., Copenhagen, 2015.

Colaizzi, P. D., Kustas, W. P., Anderson, M. C., Agam, N., Tolk, J. A., Evett, S. R., Howell, T. A., Gowda, P. H. and O'Shaughnessy, S. A.: Two-source energy balance model estimates of evapotranspiration using component and composite surface temperatures, Adv. Water Resour., 50, 134–151, doi:10.1016/j.advwatres.2012.06.004, 2012.

Detto, M., Montaldo, N., Albertson, J. D., Mancini, M. and Katul, G.: Soil moisture and vegetation controls on evapotranspiration in a heterogeneous Mediterranean ecosystem on Sardinia, Italy, Water Resour. Res., 42(8), W08419, doi:10.1029/2005WR004693, 2006.

Díaz-Varela, R. A., de la Rosa, R., León, L. and Zarco-Tejada, P. J.: High-Resolution Airborne UAV Imagery to Assess Olive Tree Crown Parameters Using 3D Photo Reconstruction: Application in Breeding Trials, Remote Sens., 7(4), 4213–4232, doi:10.3390/rs70404213, 2015.

Foken, T.: The Energy Balance Closure Problem: An Overview, Ecol. Appl., 18(6), 1351–1367, 2008.

Foken, T., Aubinet, M., Finnigan, J. J., Leclerc, M. Y., Mauder, M. and Paw U, K. T.: Results Of A Panel Discussion About The Energy Balance Closure Correction For Trace Gases, Bull. Am. Meteorol. Soc., 92(4), ES13–ES18, doi:10.1175/2011BAMS3130.1, 2011.

Fratini, G. and Mauder, M.: Towards a consistent eddy-covariance processing: an intercomparison of EddyPro and TK3, Atmospheric Meas. Tech., 7(7), 2273–2281, doi:10.5194/amt-7-2273-2014, 2014.

Gentine, P., Entekhabi, D. and Heusinkveld, B.: Systematic errors in ground heat flux estimation and their correction, Water Resour. Res., 48(9), n/a–n/a, doi:10.1029/2010WR010203, 2012.

Gonzalez-Dugo, V., Goldhamer, D., Zarco-Tejada, P. J. and Fereres, E.: Improving the precision of irrigation in a pistachio farm using an unmanned airborne thermal system, Irrig. Sci., 33(1), 43–52, doi:10.1007/s00271-014-0447-z, 2014.

Guzinski, R., Anderson, M. C., Kustas, W. P., Nieto, H. and Sandholt, I.: Using a thermal-based two source energy balance model with time-differencing to estimate surface energy fluxes with day–night MODIS observations, Hydrol. Earth Syst. Sci., 17(7), 2809–2825, doi:10.5194/hess-17-2809-2013, 2013.

Guzinski, R., Nieto, H., Jensen, R. and Mendiguren, G.: Remotely sensed land-surface energy fluxes at sub-field scale in heterogeneous agricultural landscape and coniferous plantation, Biogeosciences, 11(18), 5021–5046, doi:10.5194/bg-11-5021-2014, 2014.

Guzinski, R., Nieto, H., Stisen, S. and Fensholt, R.: Inter-comparison of energy balance and hydrological models for land surface energy flux estimation over a whole river catchment, Hydrol Earth Syst Sci, 19(4), 2017–2036, doi:10.5194/hess-19-2017-2015, 2015.

Harwin, S. and Lucieer, A.: Assessing the Accuracy of Georeferenced Point Clouds Produced via Multi-View Stereopsis from Unmanned Aerial Vehicle (UAV) Imagery, Remote Sens., 4(6), 1573–1599, doi:10.3390/rs4061573, 2012.

Herrero, J. and Polo, M. J.: Parameterization of atmospheric longwave emissivity in a mountainous site for all sky conditions, Hydrol. Earth Syst. Sci., 16(9), 3139–3147, doi:10.5194/hess-16-3139-2012, 2012.

Houborg, R., Anderson, M., Gao, F., Schull, M. and Cammalleri, C.: Monitoring water and carbon fluxes at fine spatial scales using HyspIRI-like measurements, in Geoscience and Remote Sensing Symposium (IGARSS), 2012 IEEE International, pp. 7302–7305., 2012.

Hunt Jr, E. R., Cavigelli, M., Daughtry, C. S., Mcmurtrey III, J. E. and Walthall, C. L.: Evaluation of digital photography from model aircraft for remote sensing of crop biomass and nitrogen status, Precis. Agric., 6(4), 359–378, 2005.

Jansen, J. H. A. M., Stive, P. M., Van De Giesen, N. C., Tyler, S. W., Steele-Dunne, S. C. and Williamson, L.: Estimating soil heat flux using Distributed Temperature Sensing, IAHS Publ. 343: 140-144, 2011.

Kalma, J. D., McVicar, T. R. and McCabe, M. F.: Estimating Land Surface Evaporation: A Review of Methods Using Remotely Sensed Surface Temperature Data, Surv. Geophys., 29(4-5), 421–469, doi:10.1007/s10712-008-9037-z, 2008.

Kustas, W. P. and Norman, J. M.: Use of remote sensing for evapotranspiration monitoring over land surfaces, Hydrol. Sci. J., 41(4), 495–516, doi:10.1080/02626669609491522, 1996.

Kustas, W. P., Prueger, J. H. and Hipps, L. E.: Impact of using different time-averaged inputs for estimating sensible heat flux of riparian vegetation using radiometric surface temperature, J. Appl. Meteorol., 41(3), 319–332, 2002.

Liebethal, C. and Foken, T.: Evaluation of six parameterization approaches for the ground heat flux, Theor. Appl. Climatol., 88(1/2), 43–56, doi:10.1007/s00704-005-0234-0, 2007.

Lucieer, A., Malenovský, Z., Veness, T. and Wallace, L.: HyperUAS—Imaging Spectroscopy from a Multirotor Unmanned Aircraft System, J. Field Robot., 31(4), 571–590, doi:10.1002/rob.21508, 2014.

Mauder, M. and Foken, T.: Impact of post-field data processing on eddy covariance flux estimates and energy balance closure, Meteorol. Z., 15(6), 597–609, doi:10.1127/0941-2948/2006/0167, 2006.

Moncrieff, J., Clement, R., Finnigan, J. and Meyers, T.: Averaging, detrending, and filtering of eddy covariance time series, in Handbook of micrometeorology, pp. 7–31, Springer. [online] Available from: http://link.springer.com/chapter/10.1007/1-4020-2265-4_2 (Accessed 3 June 2015), 2005.

Moncrieff, J B, Massheder, J.M., Bruin, de H., Elbers, J. A., Friborg, T. and Heusinkveld, B.: A system to measure surface fluxes of momentum, sensible heat, water vapour and carbon dioxide, J Hydrol 188189 1997 1-4 589-611, doi:10.1016/S0022-1694(96)03194-0, 1997.

Monteith, J. L.: Evaporation and environment, in Symp. Soc. Exp. Biol, vol. 19, p. 4. [online] Available from: http://www.unc.edu/courses/2007fall/geog/801/001/www/ET/Monteith65.pdf (Accessed 17 June 2015), 1965.

Norman, J. M., Kustas, W. P. and Humes, K. S.: Source approach for estimating soil and vegetation energy fluxes in observations of directional radiometric surface temperature, Agric. For. Meteorol., 77(3–4), 263–293, doi:10.1016/0168-1923(95)02265-Y, 1995.

Norman, J. M., Kustas, W. P., Prueger, J. H. and Diak, G. R.: Surface flux estimation using radiometric temperature: A dual-temperature-difference method to minimize measurement errors, Water Resour. Res., 36(8), 2263–2274, doi:10.1029/2000WR900033, 2000.

Norman, J. M., Anderson, M. C., Kustas, W. P., French, A. N., Mecikalski, J., Torn, R., Diak, G. R., Schmugge, T. J. and Tanner, B. C. W.: Remote sensing of surface energy fluxes at 101-m pixel resolutions, Water Resour. Res., 39(8), 1221, doi:10.1029/2002WR001775, 2003.

Papale, D., Reichstein, M., Aubinet, M., Canfora, E., Bernhofer, C., Kutsch, W., Longdoz, B., Rambal, S., Valentini, R., Vesala, T. and Yakir, D.: Towards a standardized processing of Net Ecosystem Exchange measured with eddy covariance technique: algorithms and uncertainty estimation, Biogeosciences, 3(4), 571–583, 2006.

Priestley, C. H. B. and Taylor, R. J.: On the Assessment of Surface Heat Flux and Evaporation Using Large-Scale Parameters, Mon. Weather Rev., 100(2), 81–92, doi:10.1175/1520-0493(1972)100<0081:OTAOSH>2.3.CO;2, 1972.

Reichstein, M., Falge, E., Baldocchi, D., Papale, D., Aubinet, M., Berbigier, P., Bernhofer, C., Buchmann, N., Gilmanov, T., Granier, A., Grünwald, T., Havránková, K., Ilvesniemi, H., Janous, D., Knohl, A., Laurila, T., Lohila, A., Loustau, D., Matteucci, G., Meyers, T., Miglietta, F., Ourcival, J.-M., Pumpanen, J., Rambal, S., Rotenberg, E., Sanz, M., Tenhunen, J., Seufert, G., Vaccari, F., Vesala, T., Yakir, D. and Valentini, R.: On the separation of net ecosystem exchange into assimilation and ecosystem respiration: review and improved algorithm, Glob. Change Biol., 11(9), 1424–1439, doi:10.1111/j.1365-2486.2005.001002.x, 2005.

Ringgaard, R., Herbst, M., Friborg, T., Schelde, K., Thomsen, A. G. and Soegaard, H.: Energy Fluxes above Three Disparate Surfaces in a Temperate Mesoscale Coastal Catchment, Vadose Zone J., 10(1), 54, doi:10.2136/vzj2009.0181, 2011.

Santanello, J. A. and Friedl, M. A.: Diurnal Covariation in Soil Heat Flux and Net Radiation, J. Appl. Meteorol., 42(6), 851, 2003.

Shuttleworth, W. J. and Wallace, J. S.: Evaporation from sparse crops-an energy combination theory, Q. J. R. Meteorol. Soc., 111(469), 839–855, 1985.

Stisen, S., Sandholt, I., Nørgaard, A., Fensholt, R. and Jensen, K. H.: Combining the triangle method with thermal inertia to estimate regional evapotranspiration — Applied to MSG-SEVIRI data in the Senegal River basin, Remote Sens. Environ., 112(3), 1242–1255, doi:10.1016/j.rse.2007.08.013, 2008.

Swain, K. C., Thomson, S. J. and Jayasuriya, H. P.: Adoption of an unmanned helicopter for low-altitude remote sensing to estimate yield and total biomass of a rice crop, Trans. ASAE Am. Soc. Agric. Eng., 53(1), 21, 2010.

Turner, D., Lucieer, A. and Watson, C.: An Automated Technique for Generating Georectified Mosaics from Ultra-High Resolution Unmanned Aerial Vehicle (UAV) Imagery, Based on Structure from Motion (SfM) Point Clouds, Remote Sens., 4(5), 1392–1410, doi:10.3390/rs4051392, 2012.

Wallace, L., Lucieer, A., Watson, C. and Turner, D.: Development of a UAV-LiDAR System with Application to Forest Inventory, Remote Sens., 4(6), 1519–1543, doi:10.3390/rs4061519, 2012.

Webb, E. K., Pearman, G. I. and Leuning, R.: Correction of flux measurements for density effects due to heat and water vapour transfer, Q. J. R. Meteorol. Soc., 106(447), 85–100, doi:10.1002/qj.49710644707, 1980.

Zarco-Tejada, P. J., González-Dugo, V., Williams, L. E., Suárez, L., Berni, J. A. J., Goldhamer, D. and Fereres, E.: A PRI-based water stress index combining structural and chlorophyll effects:

Assessment using diurnal narrow-band airborne imagery and the CWSI thermal index, Remote Sens. Environ., 138, 38–50, doi:10.1016/j.rse.2013.07.024, 2013.

Zarco-Tejada, P. J., Diaz-Varela, R., Angileri, V. and Loudjani, P.: Tree height quantification using very high resolution imagery acquired from an unmanned aerial vehicle (UAV) and automatic 3D photo-reconstruction methods, Eur. J. Agron., 55, 89–99, doi:10.1016/j.eja.2014.01.004, 2014.

Table 1 - UAV retrievals of LST, constituting 12 sets of input data to TSEB-PT and DTD. Early morning flights conducted one hour after sunrise are only used in DTD. (c) means data were collected during cloudy or overcast conditions.

		Early flights ($T_{R,0(\theta)}$)	Daylight flights ($T_{R,i(\theta)}$)				
Date		Time (UTC)					
10 April 2014	(c)	07:00			11:30		
22 April 2014	(c)	06:00					14:30
15 May 2014		05:30			11:00	12:00	
22 May 2014	(c)	05:00	08:00	09:00	11:30	12:00	
18 June 2014	(c)	05:00			11:00	12:00	
02 July 2014	(c)	07:30			11:30		
22 July 2014		06:30				12:30	

Table 2 – Changing input parameters for each flying day.

Date	LAI	Canopy height (m)	Green veg. fraction	$Albedo_{soil+veg.}$
10 April 2014	0.48	0.02	1	0.142
22 April 2014	0.88	0.08	1	0.181
15 May 2014	1.49	0.12	1	0.182
22 May 2014	3.90	0.30	1	0.226
18 June 2014	4.03	0.95	0.7	0.181
02 July 2014	3.43	1.10	0.3	0.202
22 July 2014	3.02	1.20	0.02	0.189

Comment [HHMN12]: New table showing parameters that change between each model run.

Table 3 – Measured and modelled net radiation (R_n), sensible heat flux (H), latent heat flux (LE) and soil heat flux (G). Dates marked with (c) represent days with cloudy or overcast conditions.

Comment [HHMN13]: Measured and modelled G is included

		Measured (W m^{-2})				TSEB-PT (W m^{-2})				DTD (W m^{-2})			
Date, time (UTC)		R_n	H	LE	G	Rn	H	LE	G	Rn	H	LE	G
10 April 2014 11:30	(c)	243	87	105	50	155	15	134	2	155	20	121	8
22 April 2014 14:30	(c)	203	73	81	49	180	1	181	4	180	62	118	-2
15 May 2014 11:00		453	124	241	88	401	42	330	27	401	75	295	25
15 May 2014 12:00		619	132	385	102	600	49	492	54	600	97	472	26
22 May 2014 08:00	(c)	270	33	206	31	284	-20	296	2	284	95	179	-1
22 May 2014 09:00	(c)	306	-26	290	43	301	-48	337	10	301	63	231	1
22 May 2014 11:30	(c)	406	-16	367	55	397	-33	418	14	397	101	287	6
22 May 2014 12:00	(c)	440	14	365	61	436	-51	465	21	436	42	387	4
18 June 2014 11:00	(c)	538	158	326	55	505	89	397	27	505	191	309	9
18 June 2014 12:00	(c)	631	200	378	52	612	54	514	43	612	156	450	7
02 July 2014 11:30	(c)	217	54	152	11	121	-9	135	-8	121	52	68	1
22 July 2014 12:30		479	282	161	36	511	125	335	52	511	211	293	6

Table 4 – Root mean square error (RMSE), mean absolute error (MAE) and correlation coefficient (r) computed for TSEB-PT and DTD results. Values in parenthesis are RMSE and MAE respectively as percentage (%) of measured fluxes.

	TSEB-PT			DTD		
	RMSE (W m^{-2})	MAE (W m^{-2})	r	RMSE (W m^{-2})	MAE (W m^{-2})	r
R_n	44 (11)	33 (8)	0.98	44 (11)	33 (8)	0.98
G	38 (72)	35 (66)	0.58	48 (91)	45 (86)	0.86
H	85 (91)	75 (81)	0.96	59 (64)	49 (52)	0.74
LE	94 (37)	84 (33)	0.92	67 (26)	57 (22)	0.85

Table 5 – Statistical parameters based on data that was collected during only cloudy and overcast weather conditions (9 dates). Root mean square error (RMSE), mean absolute error (MAE) and correlation coefficient (r) computed for TSEB-PT and DTD results. Values in parenthesis are RMSE and MAE respectively as percentage (%) of measured fluxes.

	TSEB-PT			DTD		
	RMSE (W m^{-2})	MAE (W m^{-2})	r	RMSE (W m^{-2})	MAE (W m^{-2})	r
R_n	40 (11)	32 (8)	0.99	40 (11)	32 (8)	0.99
G	30 (66)	33 (72)	0.66	38 (83)	42 (92)	0.61
H	63 (99)	64 (100)	0.84	53 (83)	50 (78)	0.69
LE	69 (27)	71 (28)	0.98	46 (18)	46 (18)	0.95

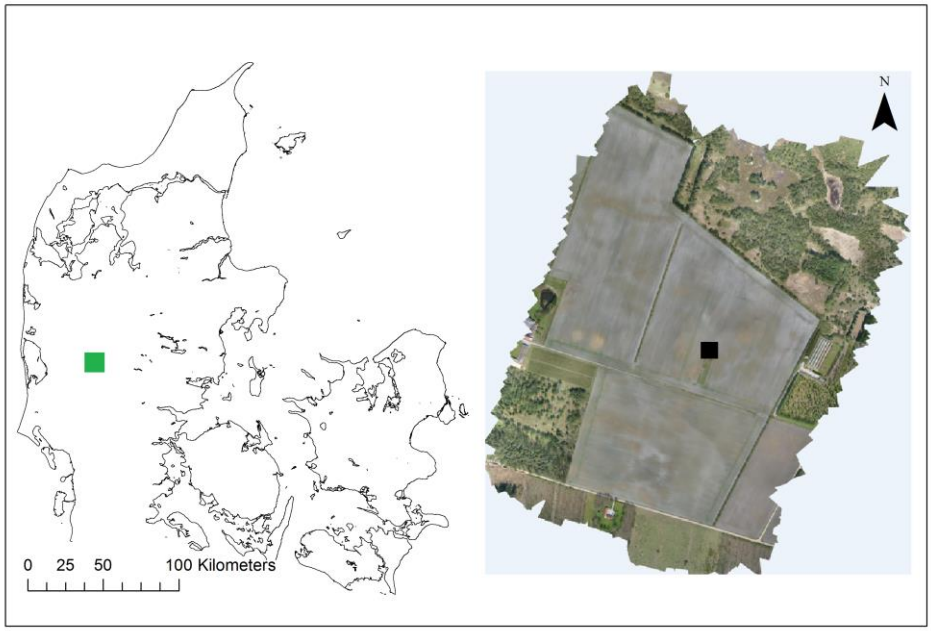

Figure 1 - HOBE agricultural site in western Denmark (56.037644°N, 9.159383°E). The black square represents location of the eddy flux tower. The green square represents location for zoom inset on the right (RGB image obtained with Lumix camera mounted on UAV).

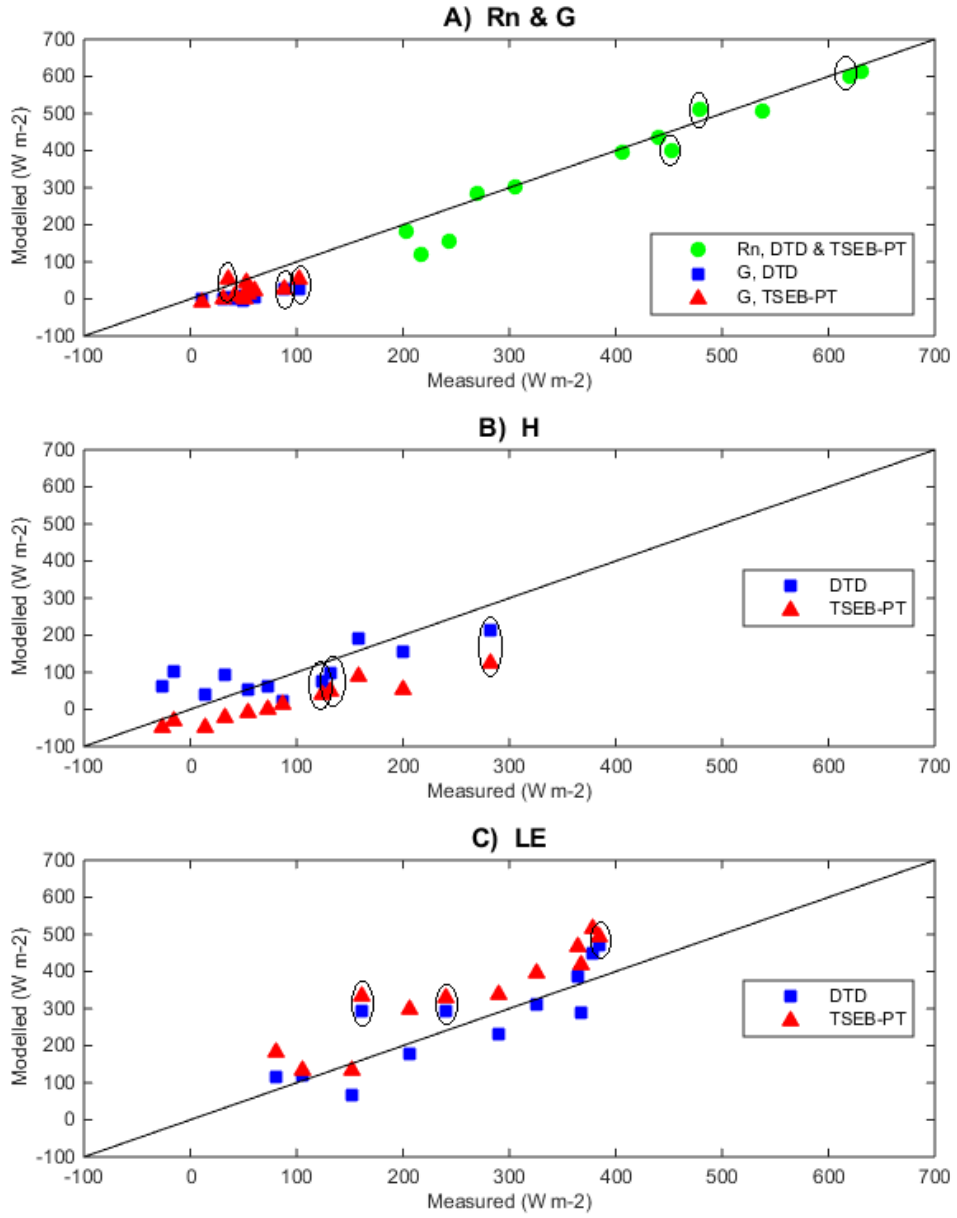

Figure 2 - Modelled vs measured net radiation (R_n), soil- (G), sensible- (H) and latent heat fluxes (LE). Data collected in sunny weather conditions are enclosed by black circles.

Comment [HHMN14]: G is included in top graph.

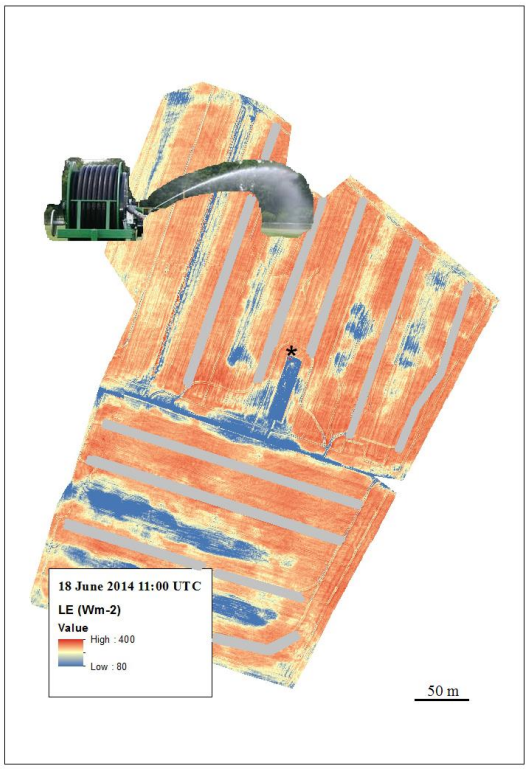

Figure 3 – Grey lines highlight tramlines in which irrigation guns are placed at all five irrigation events in 2014. The underlying map shows evaporation patterns on 18 June 2014. Red colors are high evaporation and blue colors are low evaporation. Patterns of lower evaporation correspond well with areas being furthest away from irrigation guns.

Comment [HHMN15]: This figure is included to show how repeated patterns of irrigation (provided from tramlines – grey lines) coincidence with patterns of evaporation.